

---

**PROJECT FOR THE COURSE OF FINITE ELEMENT  
METHOD, GIVEN BY PR. J.-P. PONTHOT**

# **2: The Claw**

Academic year 2021-2022

*By Bogucki Dorian, Bothorel Pierre, Boualem  
Zakaria, Rota Alberto, Sansen Damien, Scheir Tom*

---

# Contents

<b>Introduction</b>	<b>4</b>
<b>1 Strength of materials</b>	<b>5</b>
1.1 General equations of the mechanical problem . . . . .	5
1.1.1 Equilibrium equations . . . . .	5
1.1.2 Compatibility equations . . . . .	6
1.1.3 Constitutive laws . . . . .	6
1.2 Simplified hypothesis of the problem . . . . .	6
1.2.1 Support reactions . . . . .	7
1.2.2 Internal forces . . . . .	9
1.2.3 Stresses . . . . .	9
1.2.4 Vertical displacements . . . . .	11
1.3 Stress zone concentration in the literature . . . . .	12
1.4 Comments, summary and conclusion . . . . .	13
<b>2 Analysis with the Finite Element Method</b>	<b>15</b>
2.1 Rigid body modes and symmetries . . . . .	15
2.2 Modeling of the mechanical problem . . . . .	15
2.3 Types of elements . . . . .	17
2.3.1 Constant strain triangle (CST) - T3 . . . . .	17
2.3.2 Linear strain triangle - T6 . . . . .	18
2.3.3 Wilson element - Q6 . . . . .	18
2.3.4 Biquadratic element - Q8 . . . . .	19
2.4 Singularities and convergence . . . . .	19
2.4.1 Global convergence . . . . .	20
2.4.2 Local convergence . . . . .	21
2.5 Analysis of the geometry . . . . .	21
2.6 Stress tensor and boundary conditions . . . . .	22
2.7 Mesh quality . . . . .	24
2.7.1 T3 elements . . . . .	25
2.7.2 T6 elements . . . . .	25
2.7.3 Q6 and Q8 elements . . . . .	26
2.8 Sensitivity study . . . . .	27
2.8.1 Von Mises stresses . . . . .	27
2.8.2 Displacements . . . . .	28
2.9 Influence of the number of degrees of freedom . . . . .	28
2.10 Choice of the best element . . . . .	30
2.11 Maximum admissible load . . . . .	30
2.12 Advanced meshing . . . . .	31
2.12.1 Biasing on edge . . . . .	32
2.12.2 Sub-meshing . . . . .	33
<b>3 Optimization</b>	<b>37</b>
<b>Conclusion</b>	<b>39</b>

<b>List of Figures</b>	<b>41</b>
<b>List of Tables</b>	<b>41</b>
<b>References</b>	<b>41</b>

## Introduction

This project is part of the *Finite Element Method* course (MECA0036-A-b), given by Pr. Ponthot. It is asked to study a claw via a finite element approach, as represented in Fig. 0.1. The main objective is the determination of a maximum load  $\mathbf{P}$  [N] without going out of the elastic domain as well as optimizing the shape and the dimensions of the claw.

To do this, the structure imposed by the instructions will be followed. However, the order in which some subsections appear has been changed occasionally for the sake of clarity.

The first part of this report will consist in a preliminary study of the problem using a Mechanics of Materials approach : this will give a coherent order of magnitude of the maximum load  $\mathbf{P}$ . Then, simulations of different meshes (with different elements) are described. Finally, an optimization is performed : its goal is to increase the maximum admissible load  $\mathbf{P}$  while maintaining a stress field which is as uniform as possible, as well as a variation of the volume that does not exceed 5%.

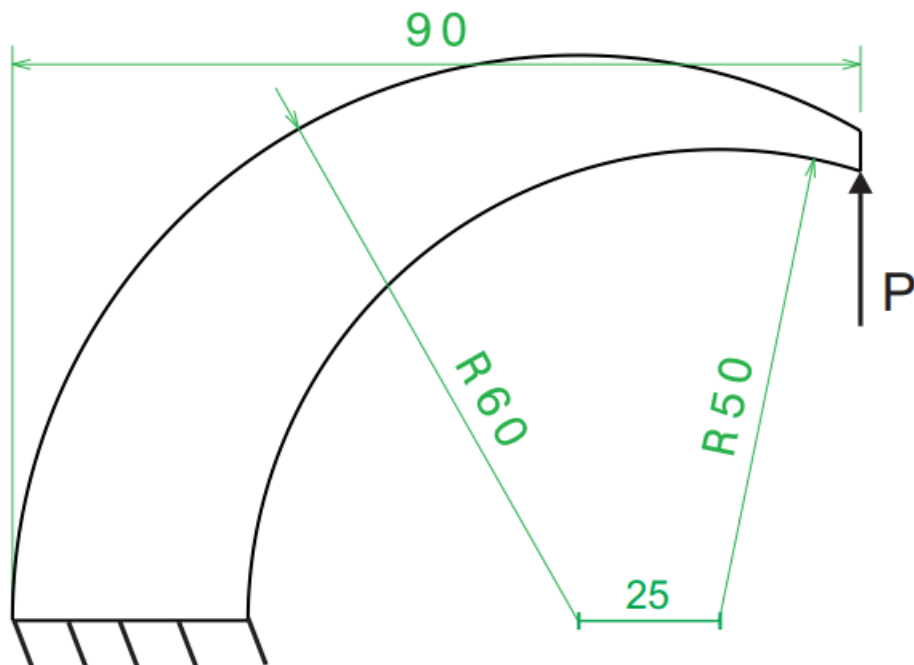


Figure 0.1: Representation of the claw (dimensions are given in mm) [1].

The parameters imposed by the problem statement are described below :

- The claw is subjected to a concentrated load  $\mathbf{P}$  at its end,
- Gravity ( $\|\mathbf{g}\| = 9.81 \text{ [m/s}^2\text{]}$ ) must be taken into account,
- The claw is clamped at its base as shown in the figure above,
- Hypothesis for analysis : plane stress state (the thickness of the claw is five millimeters),
- The material is characterized by the following properties :  $E = 400 \text{ [MPa]}$  (Young's modulus),  $\nu = 0.38 \text{ [-]}$  (Poisson's ratio),  $\sigma_y^0 = 50 \text{ [MPa]}$ ,  $\rho = 1200 \text{ [kg/m}^3\text{]}$  (density).

# 1 Strength of materials

Before developing the model, here is a reminder of the general assumptions of the mechanics of materials.

- The material is supposed to be continuous,
- The deformations are sufficiently small to remain in a purely elastic domain,
- The material is considered isotropic, linear and homogeneous,
- The problem is summarized in a state of plane stress,
- The displacements, strains and stresses are functions of the coordinates only.

Before discussing the general equations of the problem (which is the subject of the following subsection), a specific assumption about the environment need to be added : it will be assumed that the body shape can be properly distinguished from its environment. This is formalized by the following set of equations :

$$\begin{cases} S = S_u \cup S_\sigma, \\ \emptyset = S_u \cap S_\sigma, \end{cases} \quad (1.1)$$

where  $S$  denotes the total surface [-],  $S_u$  denotes the environment [-],  $S_\sigma$  denotes the body shape [-] and  $\emptyset$  is the empty set [-].

## 1.1 General equations of the mechanical problem

We can now start seeking for the exact solution of the problem. To do this, we must satisfy a set of fifteen equations either within the volume of the claw or on its surface.

### 1.1.1 Equilibrium equations

They can be divided into two categories : rotational equilibrium equations and translational equilibrium equations. The latter can be further subdivided into two subcategories : translational equilibrium in surface and translational equilibrium in volume. In total, we have respectively the equations of translation in volume, surface and rotation :

$$\frac{\partial \sigma_{ij}}{\partial x_j} + \rho \bar{b}_i = 0, \quad (1.2)$$

$$\sigma_{ij} n_j = t_i, \quad (1.3)$$

$$\sigma_{ij} = \sigma_{ji}, \quad (1.4)$$

where  $\sigma_{ij}$  are the components of the stress tensor  $\boldsymbol{\sigma}$  [Pa],  $\partial/\partial x_j$  is the partial derivative with respect to the coordinates  $x_j$  [m],  $\bar{b}_i$  are the components of the applied volume forces [ $\text{ms}^{-2}$ ],  $n_j$  are the components of the unit vector  $\mathbf{n}$  normal to the surface of the body [-] and  $t_i$  is the surface traction [Pa]. Finally, the last equation of the system results from the equilibrium of rotation and allows us to deduce the symmetry of the stress tensor  $\boldsymbol{\sigma}$ .

### 1.1.2 Compatibility equations

Under the assumption of small stresses and strains, we can deduce directly from the Green-Lagrange or Almansi tensor at order one the following relation<sup>1</sup> :

$$\varepsilon_{ij} = \frac{1}{2} \left( \frac{\partial u_i}{\partial x_j} + \frac{\partial u_j}{\partial x_i} \right), \quad (1.5)$$

where  $\varepsilon_{ij}$  are the components of the strain tensor  $\boldsymbol{\varepsilon}$  [-] and  $u_{i,j}$  are the (small) displacements [m]. This equation is oftentimes referred to as the kinematic compatibility equation.

### 1.1.3 Constitutive laws

In addition to the balance equations and the compatibility equation we just discussed, we also dispose of a series of constitutive laws, there are written here :

$$\left\{ \begin{array}{l} \sigma_{ij} = \mathbb{H}_{ijkl} \varepsilon_{kl}, \\ \mathbb{H}_{ijkl} = \lambda \delta_{ij} \delta_{kl} + G (\delta_{ik} \delta_{jl} + \delta_{il} \delta_{jk}), \\ G = \frac{E}{2(1+\nu)}, \\ \lambda = \frac{\nu E}{(1+\nu)(1-2\nu)}, \end{array} \right. \quad (1.6)$$

$$(1.7)$$

$$(1.8)$$

$$(1.9)$$

where  $\mathbb{H}_{ijkl}$  are the components of the Hooke tensor  $\mathbb{H}$  [Pa],  $\lambda$  is the second Lamé parameter [Pa] and  $G$  is the first Lamé parameter [Pa].

Eq. 1.6 allows for the linear relation between the stress tensor  $\boldsymbol{\sigma}$  and the strain tensor  $\boldsymbol{\varepsilon}$  through the fourth-order Hooke tensor  $\mathbb{H}$ . The explicit expression of the latter can, by the way, be found through Eq. 1.7 by assuming an isotropic medium. Finally, the Lamé parameters  $G$  and  $\lambda$  can be obtained through Eq. 1.8 and Eq. 1.9.

Taking account of the plane stress state approximation, we can study the deformation tensor using Voight notations, which yields :

$$\begin{bmatrix} \sigma_x \\ \sigma_y \\ \tau_{xy} \end{bmatrix} = \frac{E}{(1+\nu)(1-2\nu)} \begin{bmatrix} 1-\nu & \nu & 0 \\ \nu & 1-\nu & 0 \\ 0 & 0 & \frac{1-2\nu}{2} \end{bmatrix} \begin{bmatrix} \varepsilon_x \\ \varepsilon_y \\ \gamma_{xy} \end{bmatrix} \quad (1.10)$$

where  $\sigma_{x,y}$  are the normal stresses [Pa],  $\tau_{xy}$  are the tangential (shear) stresses [Pa],  $\varepsilon_{x,y}$  are the strains [-] resulting from  $\sigma_{x,y}$  and  $\gamma_{xy}$  are the strains resulting from  $\tau_{xy}$  [-].

## 1.2 Simplified hypothesis of the problem

Now that the basic theoretical notions have been explained, we can finally move on to our Mechanics of Materials approach. However, since the latter is based on a purely analytical solving scheme, some simplifications need to be done first.

---

<sup>1</sup>Indeed, for small stresses and strains, all strain tensors have the same expression and are equal to the Cauchy strain tensor  $\boldsymbol{\varepsilon}$ .

A first approximation we can call upon is the related to its geometry : instead of considering the shape represented in Fig. 0.1, let us use the one drawn in the schematic below.

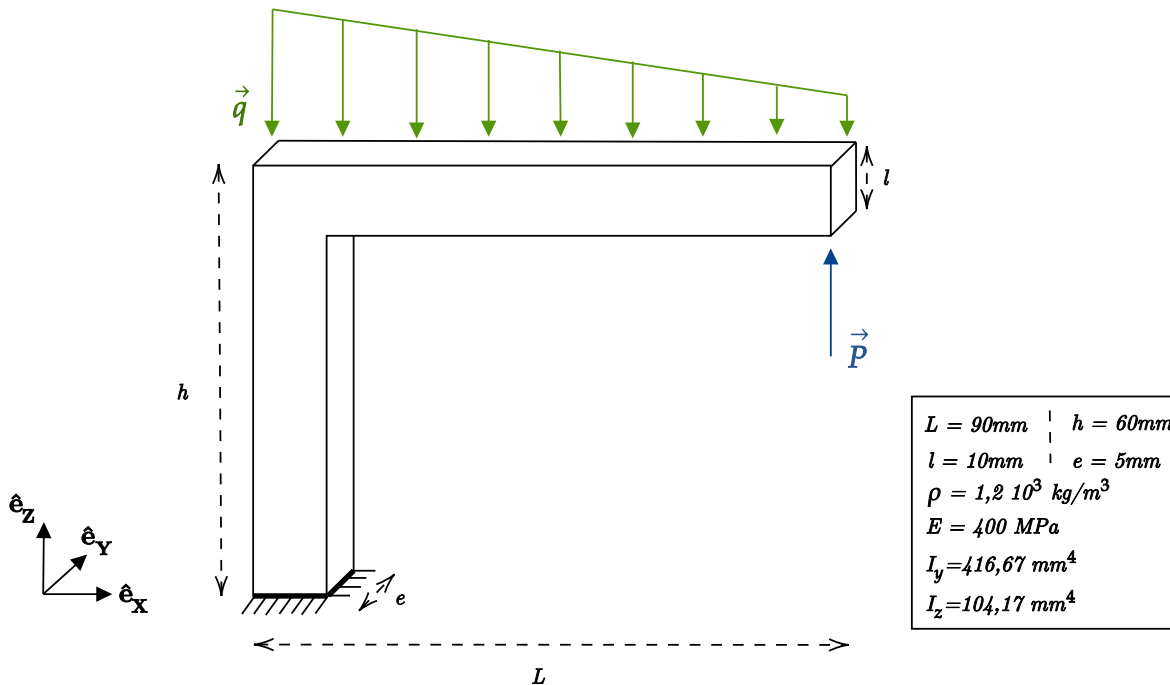


Figure 1.1: Representation of the simplified model for the use of Mechanics of Materials

This simplification consists of an L-shaped homogeneous beam which is submitted to an external loading  $\mathbf{P}$  [N] as well as its own gravity, represented by the triangular linearly distributed force  $\mathbf{q}$  [N/m]. The choice of the shape of  $\mathbf{q}$  can be justified by the fact that the force generated by gravity increases linearly with respect to the position  $x$  [m] in the horizontal part of the beam, *i.e.*  $\mathbf{q}(x) = m(x)\mathbf{g}$  where  $m(x)$  [kg/m] is the linear mass distribution.

Let us remind that the goal here is to determine the maximal admissible value for  $\mathbf{P}$  such that the subsequent deformations are linear elastic.

### 1.2.1 Support reactions

The expression of the support reactions can in theory easily be determined by writing down Newton's second law at equilibrium  $\sum \mathbf{F} = m\mathbf{a} = \mathbf{0}$  (where  $\sum \mathbf{F}$  is the sum of all forces [N] and  $\mathbf{a}$  is the subsequent acceleration [ $\text{ms}^{-2}$ ]) as well as  $\mathbf{M}^{\text{net}} = \mathbf{0}$  with  $\mathbf{M}^{\text{net}}$  the net momentum [Nm]. As stated previously, we can already identify the applied forces  $\mathbf{P}$  and  $\mathbf{q}$ . However, these are not the only forces we need to consider : we must also take into account the reaction forces  $\mathbf{V}_A$  [N] and  $\mathbf{H}_A$  [N], which are respectively the vertical and horizontal reaction forces appearing at the fixed bottom of the claw (these are represented in Fig. 1.2). Let us therefore consider the axial basis represented in this same figure ; one obtains then by projection of the forces onto the basis :

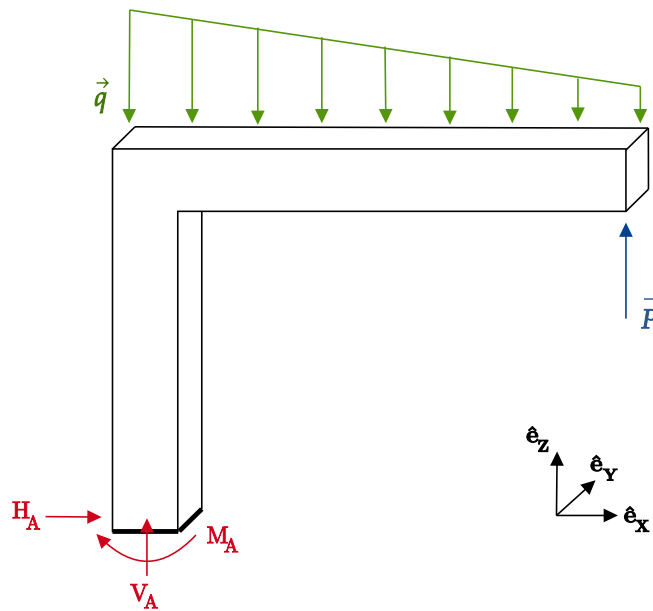


Figure 1.2: Schematic of the applied and reaction forces on the simplified claw.

$$\begin{cases} H_A = 0, \\ V_A + P - \int_0^L q(x) dx = 0, \end{cases} \quad (1.11)$$

i.e. :

$$\begin{cases} H_A = 0, \\ V_A + P = \int_0^L q(x) dx, \end{cases} \quad (1.12)$$

where  $L$  is the length of the horizontal beam. It is obvious that the integral over  $q(x)$  can be reduced to the total mass  $M_C$  [kg] of the « claw » times the module of  $\mathbf{g}$ , which will be denoted  $g$ . This yields :

$$\begin{cases} H_A = 0, \\ V_A = M_C g - P. \end{cases} \quad (1.13)$$

To get a third equation for the third unknown, let us refer to the equilibrium of momenta  $\mathbf{M}^{\text{net}} = \mathbf{0}$ . One has :

$$-M_A + PL - \int_0^L q(x)x dx = 0. \quad (1.14)$$

Given the profile of  $\mathbf{q}$ , it is obvious that one can reduce the integral above to  $1/3M_CgL$ , hence we can re-write :

$$M_A = PL - M_C g \frac{L}{3} = L \left( P - \frac{1}{3} M_C g \right). \quad (1.15)$$

### 1.2.2 Internal forces

Now that we have determined the problem is externally isostatic, we can move to the following step and seek for the expression of the internal forces  $\mathbf{T}(x)$  [N] and  $\mathbf{N}(x)$  [N], as well as for that of the internal moment  $\mathbf{M}(x)$  [Nm]. One finds that the internal forces and the internal moment can be expressed as follows in the vertical beam of the structure :

$$\begin{cases} N(x) = P - qL = -V_A, \\ T(x) = 0, \\ M(x) = PL - M_{CG}g \frac{L}{3} = M_A, \end{cases} \quad (1.16)$$

while they are expressed as follows in the horizontal beam of the structure :

$$\begin{cases} N(x) = 0, \\ T(x) = P - \frac{M_{CG}g}{L}x^2, \\ M(x) = Px - \frac{M_{CG}g}{3L^2}x^3. \end{cases} \quad (1.17)$$

In the set of equations Eq. 1.16, one notices that the module of the internal forces and that of the internal momentum are constant and equal to the absolute value of the support reactions. On the other hand, in the horizontal beam, the set of equations Eq. 1.17 shows that the internal forces depend strongly on the position  $x$  within it, as one would expect (indeed, the forces are applied to the horizontal beam according to the simplified claw model).

**Remark.** To convince ourselves of the reliability of the results, we verified that the following well known relationship :

$$\frac{dM(x)}{dx} = T(x), \quad (1.18)$$

is satisfied.

### 1.2.3 Stresses

The expressions of the internal forces being established, we can now compute the internal stresses for the structure. To do this, it is common to use the equivalent Von Mises stresses  $\sigma_{VM}$  [Pa], since they are relatively easy to compute and give an excellent estimation of the real internal stresses (provided by experimental data). Given the order of magnitude of these stresses, they will be expressed in [MPa]. By balancing out both forces and momenta, we obtain the following expressions :

$$\begin{cases} T_x = 0, \\ T_y = 0, \\ N_z = P - M_{CG}, \\ M_x = 0, \\ M_y = L \left( P - \frac{1}{3} M_{CG} \right), \\ M_z = 0. \end{cases} \quad (1.19)$$

We notice that  $T_x = T_y = M_z = 0$ , implying there are neither shear nor torsion stresses (and hence no tangential stresses). There will thus only be normal stresses (*i.e.* compression/traction) and bending stresses along the  $\mathbf{e}_y$  axis (since  $M_x = 0$ ) ; these can then be computed using the following equations :

$$\sigma_{\text{normal}} \equiv \sigma_n = \frac{N_z}{A}, \quad (1.20)$$

$$\sigma_{\text{bending}} \equiv \sigma_b = \frac{M_y z}{I_y}, \quad (1.21)$$

where Eq. 1.20 shows that the normal stress  $\sigma_n$  [Pa] is considered to be uniform along the entire cross-section of the beam and Eq. 1.21 shows that the bending stress  $\sigma_b$  [Pa] depends on both the moment of inertia  $I_y$  [ $\text{m}^4$ ] of the beam and the vertical distance  $z$  [m] from the mean fibre of the beam. These stresses are represented in the schematic below.

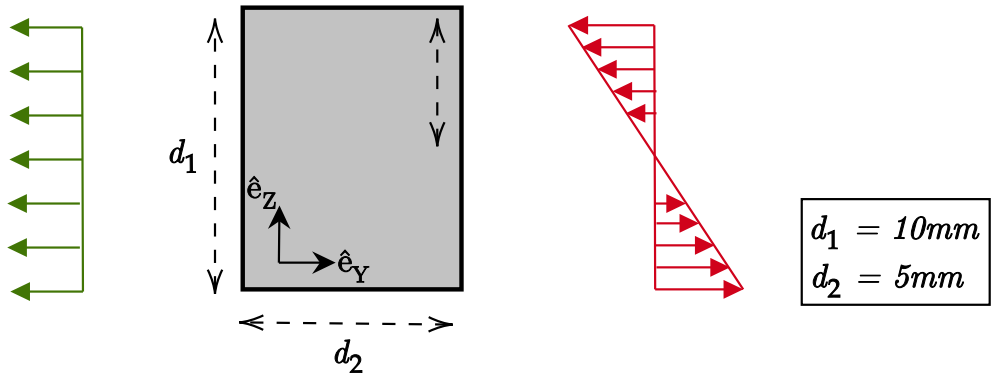


Figure 1.3: Representation of the cross-section as well as the normal stress (green) and the bending stress (red). Notice that the latter reaches its maximum at the walls of the beam.

From there, we can compute the equivalent Von Mises stresses via the following relationship :

$$\sigma_{\text{VM}} = \sqrt{\sigma_n^2 + \sigma_b^2}. \quad (1.22)$$

To render the search for the maximum admissible load  $\mathbf{P}$  as effective as possible, we developed an iterative algorithm that will be explained in the following sections.

### 1.2.4 Vertical displacements

To conclude this section, it would be interesting to find an order of magnitude of the deformations of the structure. Thus, we need to start by determining some fundamental equations for linear elastic problems. To do this, we know that when a cut is made in a two-dimensional beam, the internal forces are externalized and lead to certain deformations of the structure (**N** leads to traction/compression, **T** leads to shear and **M** leads to bending). For our simplified study, horizontal displacements of the structure will be considered negligible with respect to vertical ones and the deformations due to the bending moment **M** will be considered much greater than the ones resulting from **N** and **T**. We can thus issue a first practical equation :

$$\chi(x) = \frac{M(x)}{EI}, \quad (1.23)$$

where  $\chi(x)$  [ $m^{-1}$ ] is the curvature of the beam with respect to  $x$  and  $I$  [ $m^4$ ] is its moment of inertia with respect to its neutral axis. Assuming also small vertical displacements  $u(x)$  (this approximation holds quite well since linear elasticity can only be considered for small stresses and strains), a second equation can be found :

$$\chi(x) = -\frac{d^2u(x)}{dx^2}. \quad (1.24)$$

By comparing Eq. 1.23 with Eq. 1.24, the following fundamental equation for linear elasticity can be determined :

$$\frac{d^2u(x)}{dx^2} = -\frac{M(x)}{EI}. \quad (1.25)$$

The explicit expression of  $M(x)$  being provided by previous calculations (*cf.* Eq. 1.17), Eq. 1.25 can be re-written as follows :

$$u(x) = -\frac{1}{EI_y} \left( -\frac{M_C g}{60L^2} x^5 + \frac{P}{6} x^3 + C_1 x + C_2 \right), \quad (1.26)$$

where  $C_1$  [-] and  $C_2$  [-] are constants to be determined. To find their expression, let us consider the following boundary conditions :

$$\begin{cases} u_y(0) = 0, \\ \frac{du_y(x)}{dx} \Big|_{x=0} = 0. \end{cases} \quad (1.27)$$

One finds from there :

$$\begin{cases} C_1 = 0, \\ C_2 = 0. \end{cases} \quad (1.28)$$

Therefore one finds the following equation giving the vertical displacement  $u$  with respect to  $x$  :

$$u(x) = -\frac{1}{EI_y} \left( -\frac{M_C g}{60L^2} x^5 + \frac{P}{6} x^3 \right). \quad (1.29)$$

It is obvious that the vertical displacement will be maximum in  $x = L$  :

$$u_{\max}(x) = u(L) = \frac{1}{EI_y} \left( \frac{F_g}{60} L^3 - \frac{P}{6} L \right). \quad (1.30)$$

### 1.3 Stress zone concentration in the literature

First, a literary research was conducted to provide a reference point. Two articles will be briefly presented.

An article published by the American Journal of Veterinary Research [2] provides a comprehensive review of a bovine claw. In particular, it proceeds to take an image of the claw subjected to different static loads. The image has been reported in Fig. 1.4. It is clear that the stress area is concentrated on the tip of the claw where the load is applied, as shown by the yellow areas.

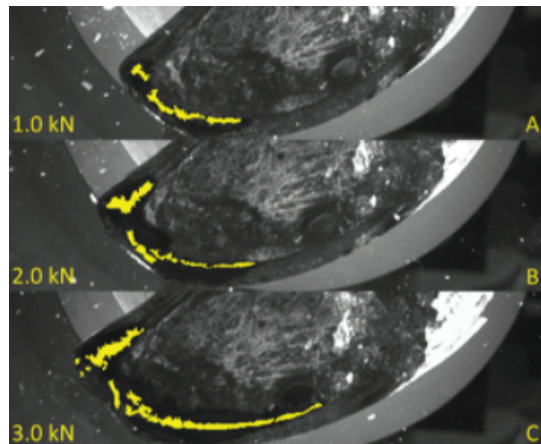


Figure 1.4: Photographic images of the bottom of a bovine hind limb claw with TTN obtained during application of a static load of 1 (A), 2 (B), and 3 (C) kN following image processing [2].

Another article presented in [3] analyzes a velociraptor claw, particularly curved. A finite element modeling is performed on the claw to study the stress field. The result is presented in Fig. 1.5. There are significant stress areas on the curved sides of the claw. The studied object is closer to that of the model which is the subject of this report.

At the end of these two articles, the literature seems to predict that the stress field of the studied claw model will be important near to the curved sides where the load is applied.

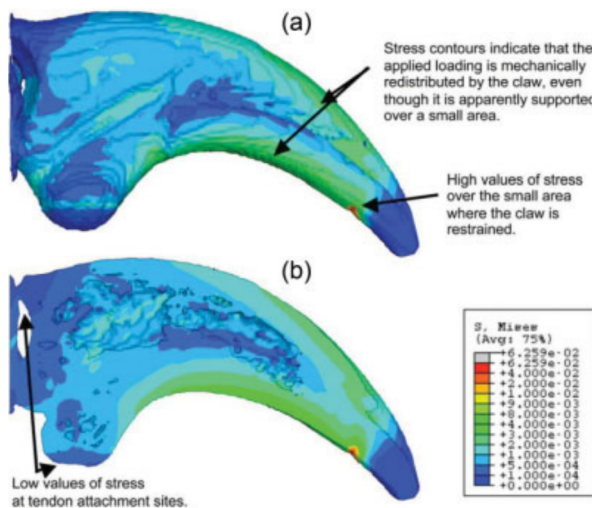


Figure 1.5: Contour map of Von Mises stresses (units in GPa) on (a) the outer surface of the claw and (b) through the mid-section [3].

## 1.4 Comments, summary and conclusion

The Mechanics of Materials approach has proven to be excessively useful for the study of our problem in an analytical manner. We have managed to obtain expressions capable of explaining and predicting how the claw will react to loads, that is the subsequent stresses and strains as well as the deformations they generate. However, we remind once more that the ease of obtaining these results has come at the expense accuracy (we will comment further on this in a moment).

In addition to interesting analytical results, a computer code has been conceived that is based on them. Thanks to this code, we can show how  $\sigma_{VM}$  behaves as a function of  $\mathbf{P}$  and hence obtain a numerical value of the maximum admissible load  $\mathbf{P}_{max}$ . Knowing that  $\sigma_y^0 = 50$  MPa according to the statement, we find  $\|\mathbf{P}_{max}\| = 46.32$  N.

As one would expect, the maximal admissible load is much greater than the gravity of the claw itself (otherwise this would mean that the claw deforms excessively under the effect of its own weight...). This also means that the deformations of the claw are virtually solely the consequence of the applied load  $\mathbf{P}$ , this is also well expected.

To finish this part of the report once and for all, let us comment some bit more on the compromise between simplicity and accuracy. As stated a few instances ago, the reason for the simplicity of our obtained analytical model comes at the expense of the accuracy of the overall result. We remind that from the beginning, we've stacked approximations : the geometry of the claw has been grossly simplified, the effects of some stresses have been neglected with respect to those of others, and so forth.

A direct consequence of this loss of accuracy can be highlighted by, for example, the results of our computer simulations (based on our obtained analytical model) : despite assuming small deformations, the ones we calculated thanks to our computer code show a maximum deviation of 33.67 mm, *i.e.* nearly 3.5 cm, which is anything but small if we compare this order of magnitude to the dimensions of the claw !

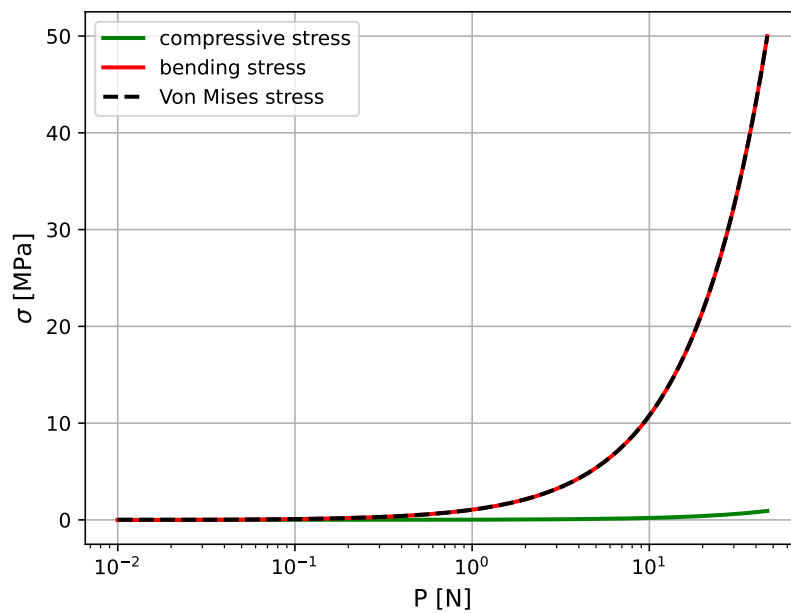


Figure 1.6: Von Mises equivalent stresses with respect to the applied load.

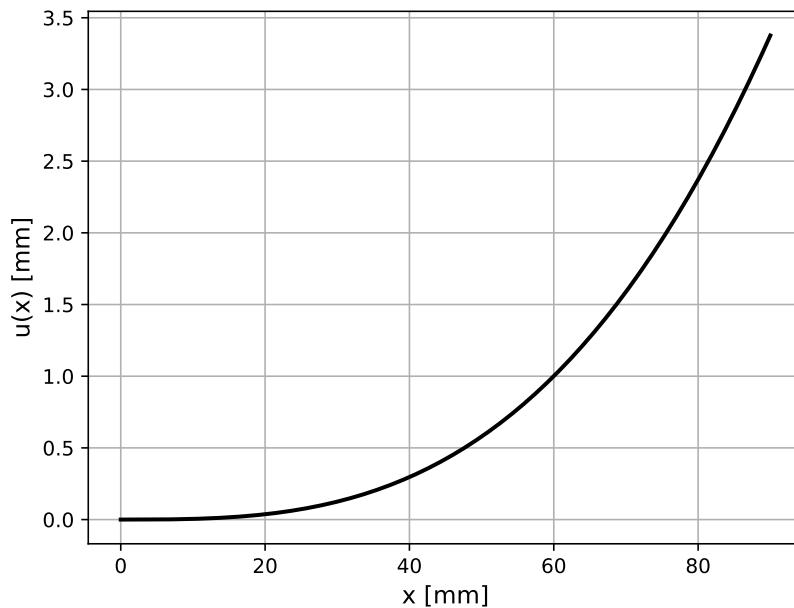


Figure 1.7: Vertical deformation of the claw resulting of applied load with respect to the position  $x$  in the horizontal beam of our simplified model.

## 2 Analysis with the Finite Element Method

### 2.1 Rigid body modes and symmetries

#### Rigid body

To study the problem correctly, we cannot consider the rigid body modes (or RBMs for short) because they represent displacements of the object without any deformation occurring. In two dimensions, there are three of them : two related to a translation of the body and one related to a rotation of the body. The boundary condition given in the statement of the problem is sufficient to suppress all the RBMs.

#### Symmetry

Our initially three-dimensional problem can be reconsidered as a two-dimensional one by analyzing a midplane. Indeed, the claw is flat and is symmetric with respect to the latter. Therefore, we can use the following plane stress assumptions :

- All loads and support conditions are midplane symmetric,
- The thickness is much smaller than the dimensions of the inplane,
- Inplane displacements, stains and stresses are uniform through thickness,
- Transverse stresses  $\sigma_{zz}$  [Pa],  $\sigma_{xz}$  [Pa] and  $\sigma_{yz}$  [Pa] are negligible.

In the plane, we can easily notice via Fig. (0.1) that it is impossible to have other symmetries which could simplify the problem further.

### 2.2 Modeling of the mechanical problem

The modeling of the mechanical problem will be performed in the CAD/FEA software Siemens NX. It can be done in a few steps for which an explanation is provided hereafter. These steps are shown in Fig. 2.1.

1. The first step of the modeling of the claw is to sketch its geometry (see Fig. 2.1a). To do this, a .prt file is needed. The claw is defined using four dimensions : the length of the claw (from left corner to right corner), the radius of curvature of the two curved edges and the distance between their center of curvature. It can also be deduced that the centers of curvature are aligned with the base of the claw. Therefore, these six constraints can be implemented in the software which allow the sketch to be fully constrained.
2. The second step is to create a surface from the geometry of the sketch (see Fig. 2.1b). This can be done using the **Fill surface** tool (indeed, it generates a surface using the lines of the sketch as its boundaries).

3. The third step is to generate a finite element mesh (see Fig. 2.1c). A `.fem` file needs to be created in order to mesh the structure. The `Mesh control` tool can be used in order to constrain the mesh on the edges of the structure. For this example, `Number on edge` has been used at the base and the tip of the claw (five elements on each edge) ; and `Biassing on edge` on the curved edges (forty elements on each edge with a bias ratio of 0.94). Then, the `2D mapped mesh` tool has been used to create a mesh of Q6 elements.
4. The fourth step is to specify the loads and boundary conditions of the simulation to the solver (see Fig. 2.1d). A `.sim` file needs to be created in order to specify these conditions. Here, there are two loads : the load applied on the upper right corner and the acceleration of the whole body due to gravity. There is also a fixed constraint on the base of the claw as it is fixed on the ground.
5. Finally, the simulations can be started and the results can be analyzed. This process will be explained thoroughly in the following sections.

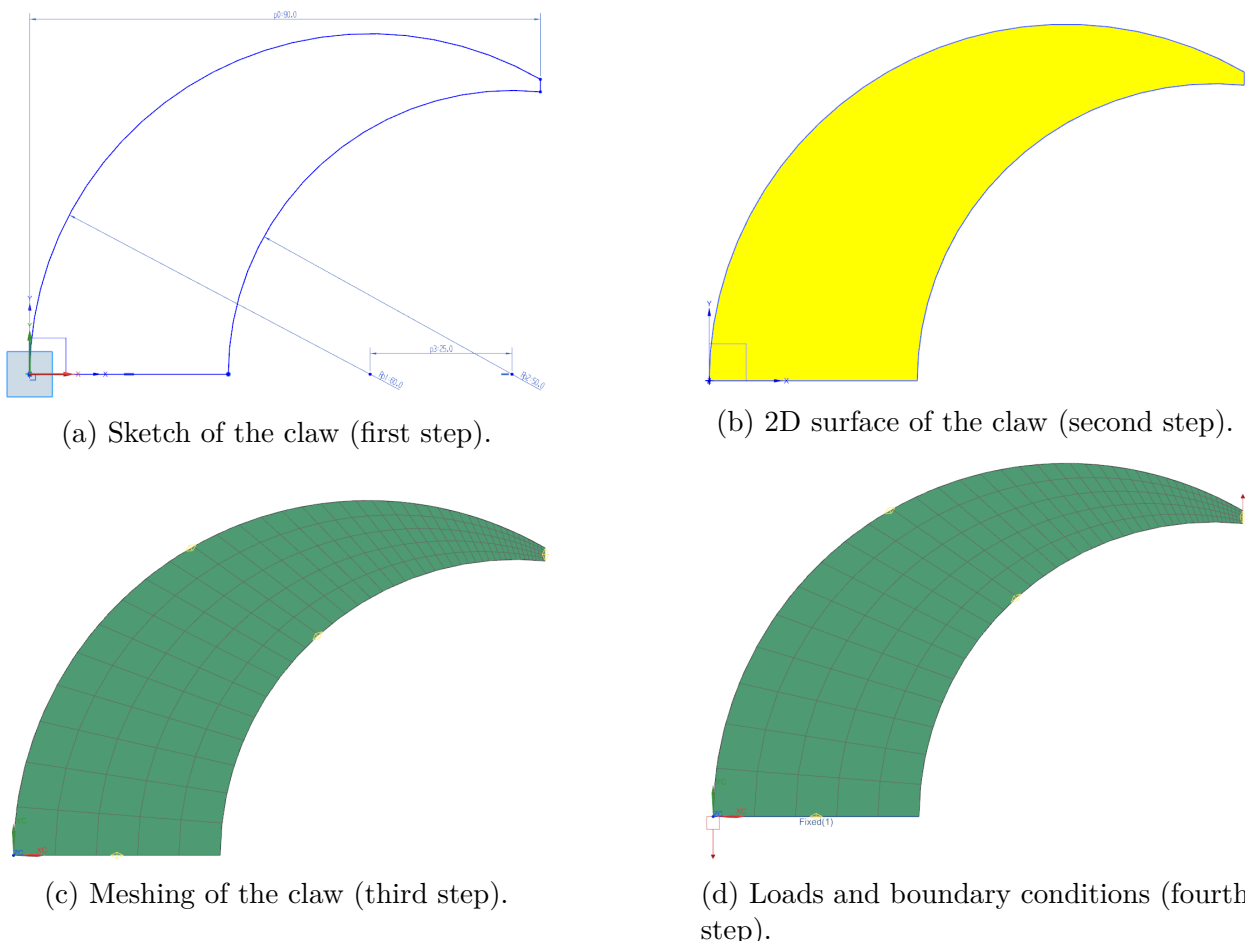


Figure 2.1: Modeling of the claw using Siemens NX.

## 2.3 Types of elements

To understand the next paragraphs, it is important to recall a few points of the theoretical lectures [1]. In the Finite Element Method, we do not know *a priori* the expression of the displacements ; instead, we try to approximate them with a polynomial expression. Thus, we have that the displacements is composed of a multiplication between factors  $\alpha_i$  [-] called internal parameters and modes (the different degrees of the polynomial) as shown by the following expression :

$$\mathbf{u}(x) = \alpha_0 + \alpha_1 x^1 + \alpha_2 x^2 + \dots + \alpha_n x^n = \mathbf{P}\mathbf{a}, \quad (2.1)$$

where  $\mathbf{P}$  is the matrix of polynomial modes and  $\mathbf{a}$  is the internal parameter vector [-].

In addition to that, we impose the continuity of displacements from one element to another. Because of this, we must use connectors (which are the components of the nodal vector  $\mathbf{q}$ ). Furthermore, we assume that the displacement field  $\mathbf{u}$  (also valid inside the element) must be compatible with them. Mathematically, we can illustrate this by the following relation :

$$\mathbf{q} = \mathbf{u}(x, y, z)|_{\text{connectors}} = \mathbf{P}|_{\text{connectors}}\mathbf{a} = \mathbf{Q}\mathbf{a} \iff \mathbf{a} = \mathbf{Q}^{-1}\mathbf{q}, \quad (2.2)$$

where  $\mathbf{Q}$  is the matrix of polynomial modes at the nodes. One also has :

$$\mathbf{u}(\mathbf{x}) = \mathbf{P}(\mathbf{x})\mathbf{a} = \mathbf{P}(\mathbf{x})\mathbf{Q}^{-1}\mathbf{q} = \mathbf{N}(\mathbf{x})\mathbf{q}, \quad (2.3)$$

where  $\mathbf{N}(\mathbf{x})$  is the shape function matrix.

We can deduce from these two equations Eq. 2.2 and Eq. 2.3 that  $\mathbf{Q}$  must be invertible (such that it is square and linearly independent) to get the shape function matrix. Therefore, a necessary condition is that the number of connectors is equal to the number of internal parameters.

### 2.3.1 Constant strain triangle (CST) - T3

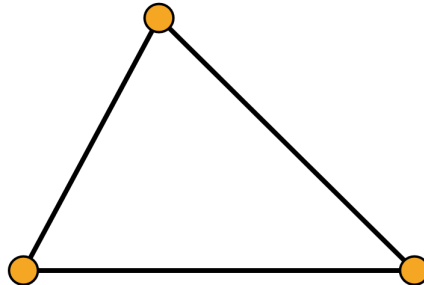


Figure 2.2: Schematic of the T3 finite element.

The so-called constant strain triangle (or CST for short) is the simplest of the 2D elements. It has three nodes and therefore six degrees of freedom (or DOFs for short) (connectors). We assume a linear displacement :

$$\begin{cases} u(x, y) &= \alpha_1 + \alpha_2 x + \alpha_3 y, \\ v(x, y) &= \beta_1 + \beta_2 x + \beta_3 y, \end{cases} \quad (2.4)$$

where  $u(x, y)$  and  $v(x, y)$  are respectively the horizontal and vertical deformations and both depend on the coordinates  $(x, y)$ . We have six internal parameters  $(\alpha_i, \beta_i)$  for six connectors and thus the element validates one of the necessary conditions. It must also be linearly independent, however, this cannot be deduced from a general case.

The deformation of this element can be computed quite easily since it follows a linear relationship for the displacement. Knowing also that the deformation derives from the displacement as shown in Eq. 1.5, we get constant deformations related only to internal parameters.

### 2.3.2 Linear strain triangle - T6

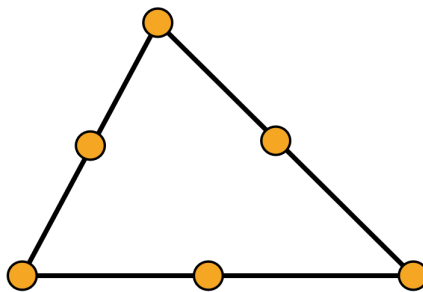


Figure 2.3: Schematic of the T6 finite element.

This element has six nodes (and thus twelve DOFs). In contrast with the T3 element, the displacements  $u$  and  $v$  are considered to be quadratic instead of linear, *i.e.* :

$$\begin{cases} u(x, y) = \alpha_1 + \alpha_2x + \alpha_3y + \alpha_4x^2 + \alpha_5xy + \alpha_6y^2, \\ v(x, y) = \beta_1 + \beta_2x + \beta_3y + \beta_4x^2 + \beta_5xy + \beta_6y^2. \end{cases} \quad (2.5)$$

This gives twelve internal parameters for twelve connectors. This element is also valid (we also speak of being kinematically admissible) for the same reason as previously. Finally, the deformation of this element is not constant but linear due to second order displacements.

### 2.3.3 Wilson element - Q6

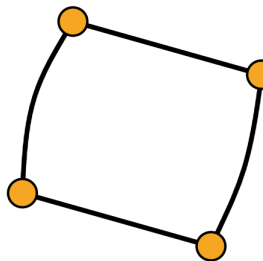


Figure 2.4: Schematic of the Q6 finite element.

Wilson Q6 elements are used by default in a vast majority of commercial finite element softwares. However, they are called Q4 in many of them. This is the case for Samcef which is the FEM solver used in the work.

Since the Wilson (Q6) element is based on the bilinear quadrilateral element (Q4), the latter needs to be introduced first. It has four nodes and its displacement field is given as follows:

$$\begin{cases} u(x, y) = \alpha_1 + \alpha_2x + \alpha_3y + \alpha_4xy, \\ v(x, y) = \beta_1 + \beta_2x + \beta_3y + \beta_4xy. \end{cases} \quad (2.6)$$

The Wilson Q6 element has two additional DOFs with respect to the Q4 element that are not connected to adjacent elements. Its displacement field is given by :

$$\begin{cases} u = \sum_{I=1}^4 N^I u^I + \left( \frac{1 - (x/a)^2}{2} \right) u^5 + \left( \frac{1 - (y/b)^2}{2} \right) u^6, \\ v = \sum_{I=1}^4 N^I v^I + \left( \frac{1 - (x/a)^2}{2} \right) v^5 + \left( \frac{1 - (y/b)^2}{2} \right) v^6, \end{cases} \quad (2.7)$$

where the first sum comes from the Q4 element,  $2a$  is the length of the element and  $2b$  is its height. These two additional DOFs allow for parabolic displacements at the edges of the element. The Q6 element produces incompatible modes (*i.e.* there are gaps between the elements). Therefore, the FEM software needs to check the convergence (Patch test).

### 2.3.4 Biquadratic element - Q8

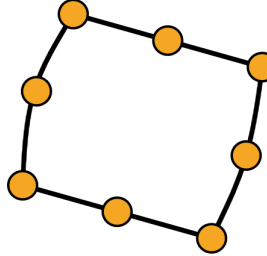


Figure 2.5: Schematic of the Q8 finite element.

Simple quadrilateral elements can be extended in order to exhibit a quadratic displacement profile on the edge by introducing one additional node at the midpoint of each edge. Without the introduction of a supplementary node in the middle of the quadrilateral (which is the case for the Q9 element), the displacement field for Q8 has the form :

$$\begin{cases} u(x, y) = \alpha_1 + \alpha_2x + \alpha_3y + \alpha_4x^2 + \alpha_5xy + \alpha_6y^2 + \alpha_7x^2y + \alpha_8xy^2, \\ v(x, y) = \beta_1 + \beta_2x + \beta_3y + \beta_4x^2 + \beta_5xy + \beta_6y^2 + \beta_7x^2y + \beta_8xy^2. \end{cases} \quad (2.8)$$

The equations for Q8 are both smooth, continuous and complete to degree 1, assuring convergence for this element.

## 2.4 Singularities and convergence

The finite element method is an approximation of reality. It allows to have a strong knowledge of the displacements inside the element. On the other hand, we have a weak knowledge of

the constraints. Indeed, we can only have a knowledge of the average stresses from one element to another. This weak knowledge of stresses allows for stress discontinuities at the nodes. Thus, it is important to check that there are no stress discontinuities at the different nodes generating singularities so that our results are not biased.

In our case, for modeling the applied load  $\mathbf{P}$ , we have two possibilities : either the force is punctual and applied directly on the last node in question, or the force is applied on a certain section of the claw. In order to choose between them, we studied their global and local convergence to ensure that there are no singularities or other problems in the simulation. Due to the small size of our object, we decided to study its convergence for element sizes of 5 mm, 2 mm, 1 mm, 0.5 mm and finally 0.2mm.

#### 2.4.1 Global convergence

For the global convergence, we studied the total potential energy (TPE) as a function of the size of the elements. Indeed, it is obvious that if the TPE diverges, the simulation is inherently troublesome.

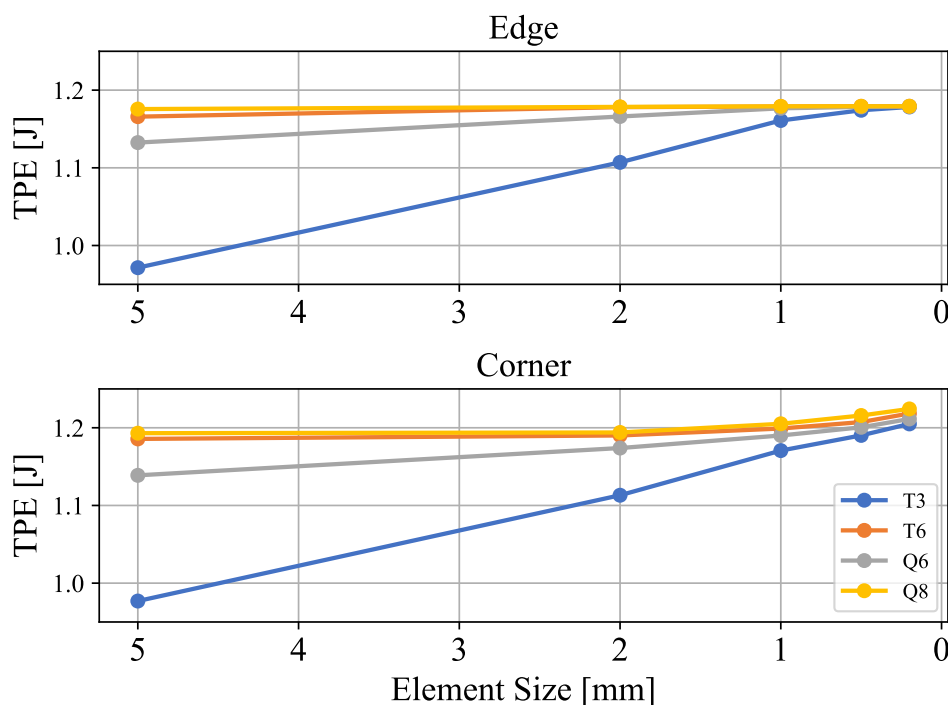


Figure 2.6: Global convergence - TPE as function of the element size.

We can observe that our two situations converge well and moreover, towards the same value. This means that in any case the global convergence is guaranteed and that our simulations work on average.

**Remark.** It is interesting to note that both the T6 and the Q8 elements seem to converge to the actual value of the TPE from the very beginning, *i.e.* regardless of the size of the element. In contrast, this is not the case for the T3 and Q6 elements (they only start to converge to the actual value of the TPE later on).

### 2.4.2 Local convergence

As said earlier, there is a good knowledge of the displacements but a weak knowledge of the constraints. Thus, the local convergence is studied to make sure that there is no singularity in the Von Mises stresses for both situations.

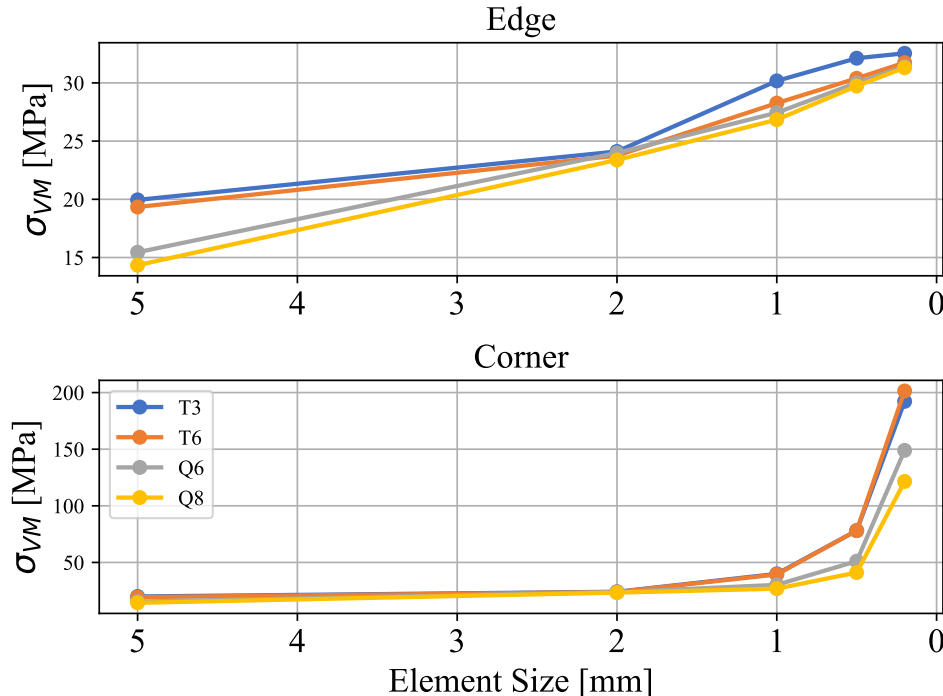


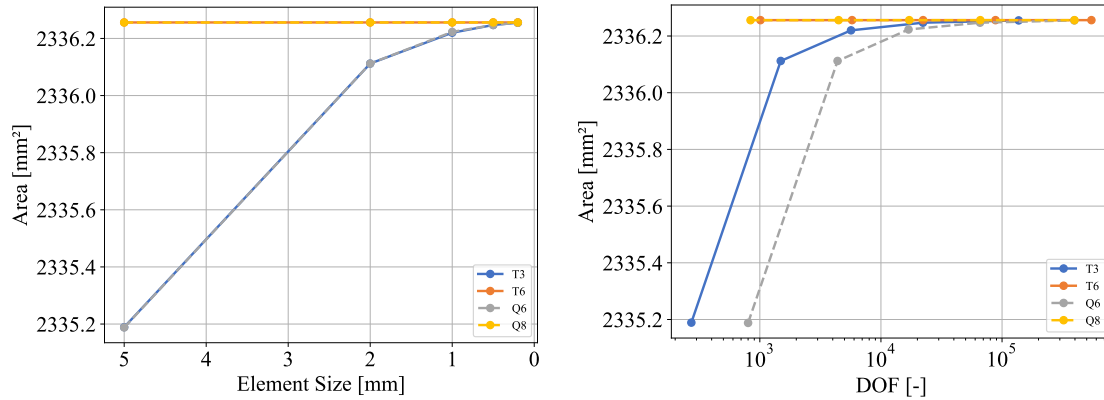
Figure 2.7: Local convergence -  $\sigma_{VM}$  as a function of the element size.

As expected, the values of  $\sigma_{VM}$  either converge or diverge, according to the positioning of the applied load  $\mathbf{P}$ . For the case in which the latter is applied on the corner, there is a singularity which can be due to the fact that the force is applied on a single node. Therefore, from now, only the case where the force is applied on the edge will be considered in order to avoid singularities that could bias the results.

## 2.5 Analysis of the geometry

The elements having a shape and a size that we impose, the geometry can be affected and consequently, our results. In order to avoid this, we looked at the convergence of the geometry as a function of the size of the element and the number of degrees of freedom. Being in a constraint plane, we can characterize the geometry by the area of our claw. The volume is simply the result of the area multiplied by the thickness which is 5 mm in our case. Thus the tendency of the following graphs are identically found in those of the volume.

Fig. 2.8a is linked to the geometry of the claw with respect to the size of the element. Indeed, there is a convergence of the area for the T3 and Q6 elements towards a finite value while there is a line (no variation) for the T6 and Q8 elements. The different trends of the lines connecting the points can be explained as follows. The T3 and Q6 elements are linear



(a) Computed area of the claw with respect to the element size.  
(b) Computed area of the claw with respect to the number of degrees of freedom.

elements, *i.e.* they simply have points at the different nodes, which means that the sides are rigid and cannot be deformed to fit the body geometry we impose. In contrast, both the T6 and Q8 elements have additional nodes placed at the median of each side of the element, which allow a better deformability of the element and therefore, a better adaptation to the geometry of the structure.

Fig. 2.8b shows the area representing the geometry as a function of the number of degrees of freedom. This choice can be explained by the fact that a type of element of fixed size does not necessarily have the same number of degrees of freedom as another type of element for that same size. It is therefore interesting to study this behavior through this graph. We notice that, as was the case for the element sizes, the area for both the T6 and Q8 elements does not vary. The explanation for this is the same as in the previous paragraph. For the two other types, we notice a convergence of the area but with a translation more to the right for the curve of the Q6 element with respect to that of the T3 element. This is expected since the Q6 element, being quadrilateral, has a number of degrees of freedom which is greater than that for a T3 element of the same size.

Finally, we established a table showing the real value of the area and the ones obtained with the different types of elements. Whatever the element, for an element size of 0.2mm, there is almost equivalence with the real area.

	Real value	T3	T6	Q6	Q8
Surface [mm <sup>2</sup> ]	2336.2559	2336.2550	2336.2560	2336.2550	2336.2559

Table 2.1: Surface of the claw as approximated by meshing with different elements

## 2.6 Stress tensor and boundary conditions

Before going any further, it was decided to check the spatial distribution of the different components of the stress tensor as well as the boundary conditions in order to ensure that they are correctly respected. Indeed, a simulation can give a result, but if there is no engineer behind it to confirm their viability, they are inherently worthless.

We will start directly with the constraints. Since a plane stress state is considered, the  $z$  components of the stress tensor  $\sigma$  are obviously equal to zero. The  $\sigma_{xx}$  and  $\sigma_{yy}$  components

correspond respectively to the tension/compression stresses in the  $x$  and  $y$  direction at this location and will play a major role in the determination of the Von Mises stresses. Indeed, the  $\sigma_{xy}$  components represent the shear stresses, which are present but much weaker than the former. We can find this same reasoning in our Mechanics of Materials approach, for which we had a geometry which did not consider any tangential stresses (obviously, this latter consideration is no longer valid for the claw due to its inclined extremity (this will generate shear)). Finally, one can be assured of the reliability of the simulations by comparing them to Fig. 1.5 where the stress concentration areas appear on the sides of the claw, while they are almost zero at the end and at the anchor.

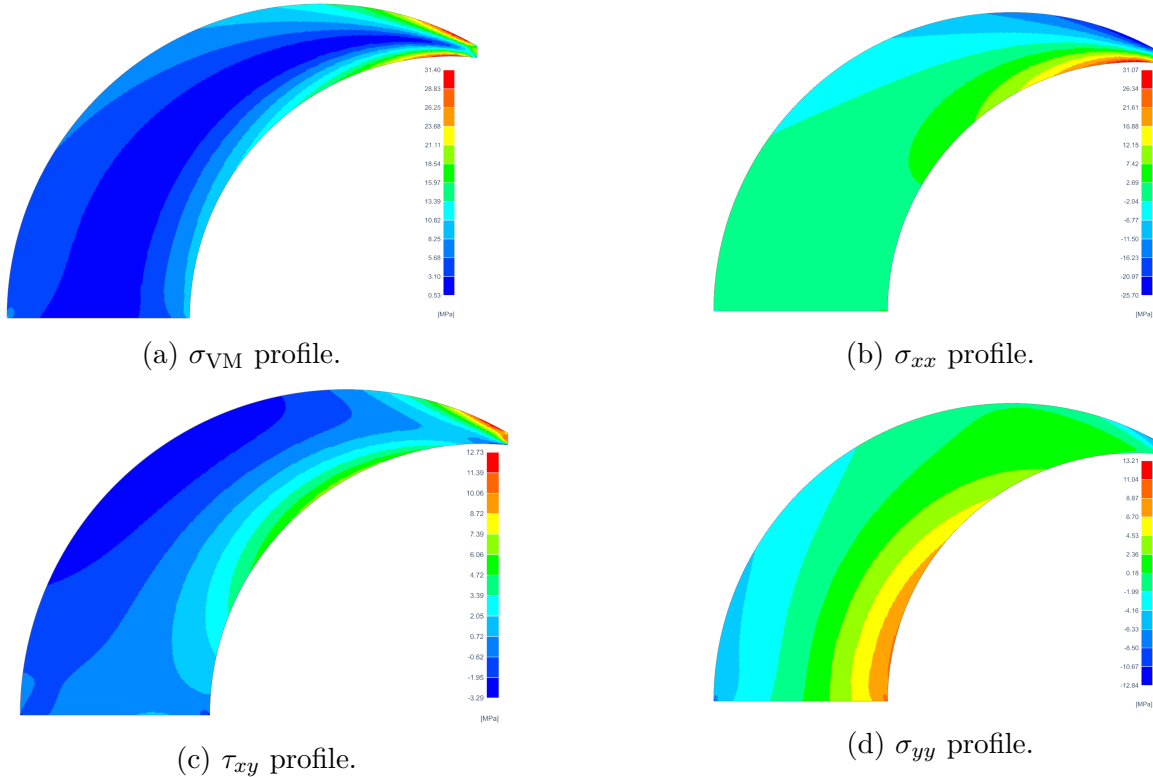


Figure 2.9: Modeling of the various stress components with NX.

We continue by examining the displacement which must obviously be zero at the anchorage. We obtain Fig. 2.10 which confirms this condition. Furthermore, as was predicted by our Mechanics of Materials approach, the further we move to the tip of the claw, the greater its deformation. It is also interesting to see that the order of magnitude of the maximal value for this deformation is the same as the one predicted by our simplified model ( $\sim$  one centimeter), even though those calculations yielded results that were in direct contradiction with our approximations !

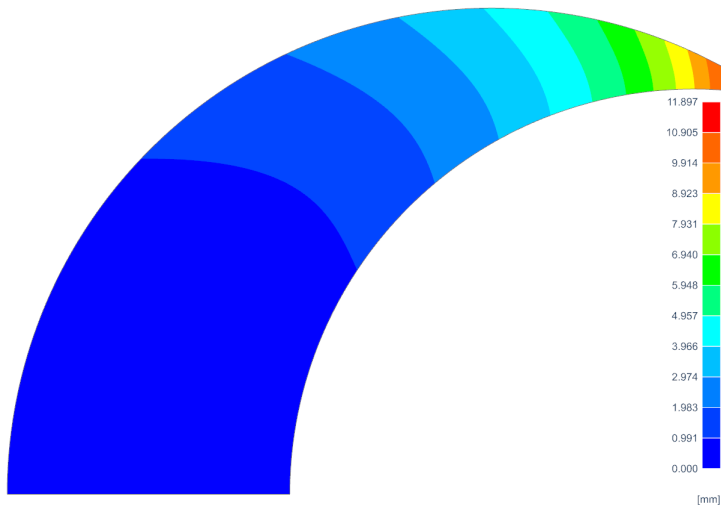


Figure 2.10: Displacement profile in the claw according to our NX simulations.

## 2.7 Mesh quality

In order to check the quality of the mesh generated for any type of element (T3, T6, Q6 and Q8), different NX tools will be used. This mesh quality allows one to get a great first insight in choosing the best element for the claw. Because of the very simple meshes, this study is preliminary and should therefore be considered as such. It will give an order of magnitude of the element size needed, the particularities of triangle and square elements, and in which parts of the structure the element particularly deformed. NX proposes a wide variety of interesting tools that could help us with this task, such as the Jacobian sign, the Jacobian ratio, the aspect ratio, the skew angle and maximum/minimum interior angles. Their definitions are given below.

**Jacobian sign.** This sign is determined for every element. If it is not the same for all elements, the simulation must fail. Thus, the condition is verified if and only if the sign of the Jacobian is always the same. Elsewhere, the geometry must be eliminated.

**Jacobian ratio.** Ratio between the largest and smallest value of the Jacobian determinant of the element. This ratio expresses the quality of an element by comparing its shape with that of an ideal one. Therefore, the ideal Jacobian ratio value is 1. It can also be smaller than 1 and even negative. A negative aspect ratio causes the analysis program to stop (*cf.* previous definition).

**Aspect ratio.** Ratio between the longest element edge and the shortest element edge. Indeed, this ratio is the measure of a mesh element's deviation from having all sides of equal length. Therefore, the aspect ratio of an equilateral triangle element and a square element are equal to 1, which is the ideal value. We usually use elements with aspect ratios smaller than three ; above this value, the element will be considered too long or too thin, which will decrease the overall accuracy of the simulation.

**Skew angle.** The skew angle is defined in two different ways depending on whether the

elements are triangular or quadrilateral.

- In a triangular element, the skew angle is related to the four angles formed by the intersection of two lines, one by linking one vertex of the triangle to the midpoint of its opposite side, and the other by linking the midpoints of the other two sides of the triangle. This process is repeated for all three vertices, for a total of twelve angles. Thus, the skew angle is defined as ninety degrees minus the minimum of the twelve angles.
- For a quadrilateral element, we first find the minimum of the four angles formed by the two lines joining the opposite midpoints of the elements. Ninety degrees minus the minimum of the four angles defines the skew angle for the four-node element.

The generally accepted skew angle lower than forty-five degrees. These two definitions are taken from the book Basic Finite Element Method as Applied to Injury Biomechanics in section 3.8.2 edited by King-Hay Yan [4].

**Maximum and minimum interior angle.** These angles represent the internal angles formed by any two edges of the element. In general, acceptable degrees range from 30 to 120 degrees for triangles and from 45 to 135 for quadrilaterals. These parameters, as well as others previously mentioned, allow us to estimate the deformation of the elements with respect to the initial geometry.

We plotted an automatic mesh of the structure with different element types (T3, T6, Q6 and Q8) and with different element sizes (2 mm, 1 mm, 0.5 mm and 0.2 mm) and we checked for the worst values for the defined parameters for all the elements of the structure. The following results are obtained.

### 2.7.1 T3 elements

Element size	Jacobian sign	Jacobian ratio	Aspect ratio	Skew angle	Min angle	Max angle
2 mm	verified	1	2.17	40.41	33.74	101.65
1 mm	verified	1	2.62	48.27	28.01	111.59
0.5 mm	verified	1	1.77	32.76	36.15	89.96
0.2 mm	verified	1	2.25	44.17	29.66	100.59

Table 2.2: Worst values of element quality parameters for T3 elements.

### 2.7.2 T6 elements

Element size	Jacobian sign	Jacobian ratio	Aspect ratio	Skew angle	Min angle	Max angle
2 mm	verified	1.03	2.17	40.41	33.74	101.65
1 mm	verified	1.02	2.62	48.27	28.01	111.59
0.5 mm	verified	1.01	1.77	32.76	36.14	89.96
0.2 mm	verified	1.00	2.25	44.17	29.66	100.58

Table 2.3: Worst values of element quality parameters for T6 elements.

We can already notice that the T3 and T6 elements have truly similar geometrical properties. However, the best element seems to be the 0.5 mm one. Indeed, its Jacobian ratio is 1 and its aspect ratio and skew angle are very close to the values of that of an ideal element. Overall, this must mean that the accuracy of the simulations will be greatly improved.

We will now examine the square elements Q6 and Q8. Let us note that the automatic meshes have been plotted without any triangular element (using the tool **Zero triangle**).

### 2.7.3 Q6 and Q8 elements

Element size	Jacobian sign	Jacobian ratio	Aspect ratio	Skew angle	Min angle	Max angle
2 mm	verified	2.98	1.51	30.27	45.79	138.56
1 mm	verified	2.94	1.44	33.16	47.89	139.02
0.5 mm	verified	4.01	1.74	38.01	40.85	142.76
0.2 mm	verified	3.64	1.53	33.34	47.96	142.95

Table 2.4: Worst values of element quality parameters for Q6 and Q8 elements.

The Q6 and Q8 elements yield the exact same results. Referring to the values of the table, we realize that the best element is the one with 1 mm of element size.

Then, we can compare the square elements Q6 and Q8 with the triangular ones T3 and T6. We notice that the Jacobian ratios are three and sometimes four times higher for the square elements with respect to the triangular ones. Nevertheless, these values remain acceptable. Other geometrical values such as aspect ratio and angles are much better for the Q6 and Q8 elements.

Thus, we determined that it is preferable to use square elements, particularly for this simple geometry. Indeed, even if the triangular element can more easily fit excessively complex geometries<sup>2</sup> than its quadratic counterpart, the stresses they yield are less accurate. Here, the geometry is simple, so there's no real disadvantage in using Q6/Q8 elements.

Now, we can analyse the localisation of the meshing errors. To do so, we plot an automatic mesh for both the T6 and Q6 elements with a 0.2 mm element size (see Fig. 2.11). Let us note that the T6 and Q6 elements are used for the illustration since their geometrical parameters are very close respectively to the T3 and Q8 elements. The restrictions we used have been chosen accordingly to the worst values determined before. We have used the **Warning** value just below the worst value to determine where the troublesome elements are located within the structure : we can notice that they are concentrated at the center of the structure. More specifically, for the Q6 elements, the problematic elements are located at the center just above the basis of the claw. However, knowing the stresses are majorly concentrated on the extremity of the claw, the ones generated at the basis can be considered negligible. Therefore, we can perfectly use a square element for the meshing because the deformations, as well as the loss of accuracy for the stress computation, will be negligible. Actually, we might even use larger elements to mesh the basis in reduce the computing time (one would say that this will impact the accuracy of the solution, which is correct ; however, since

<sup>2</sup>By the way, it can be proven by mathematicians that one can mesh any geometry, as complex as one can imagine, with tetrahedrons, which is not true for parallelepipeds !

nothing interesting happens at the base of the claw, we can live with that sacrifice). Finally, it can be concluded that the square element is well adapted for this problem. The worst values of the diverse criteria are totally acceptable and the elements which are submitted to the largest deformations are concentrated in areas where the stresses are small.

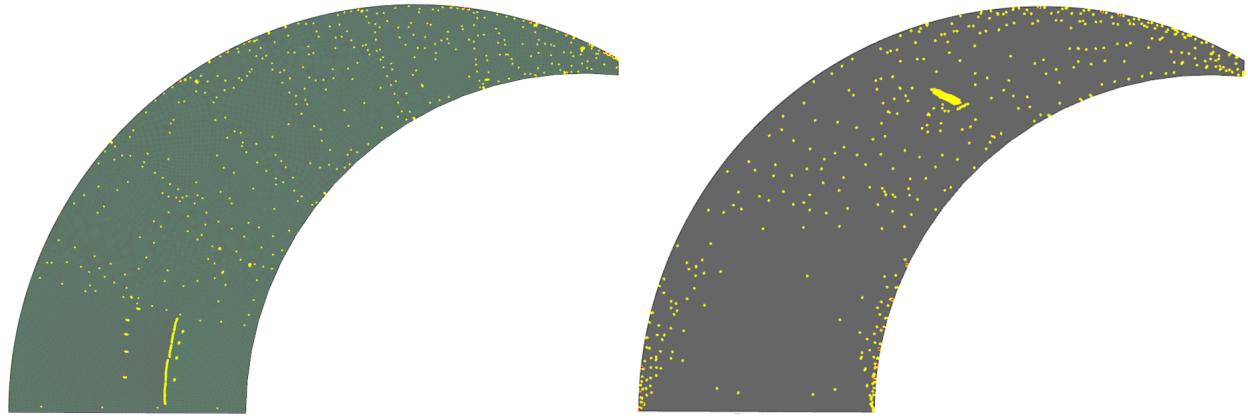


Figure 2.11: Aberrant elements in a mesh with Q6 elements (left) and T6 elements (right).

## 2.8 Sensitivity study

The important and primordial aspect of this work is the primary analysis (for a coarse mesh) of the parameters, be it the stresses or the displacement of the tip of the claw. To do this, we have established different graphs showing either the Von Mises constraints or the displacement as a function of the size of the element and the number of degrees of freedom. This last parameter is very important because it characterizes quite well the CPU computation time. The correlation between the number of degrees of freedom and the CPU time will be shown in the next sections.

### 2.8.1 Von Mises stresses

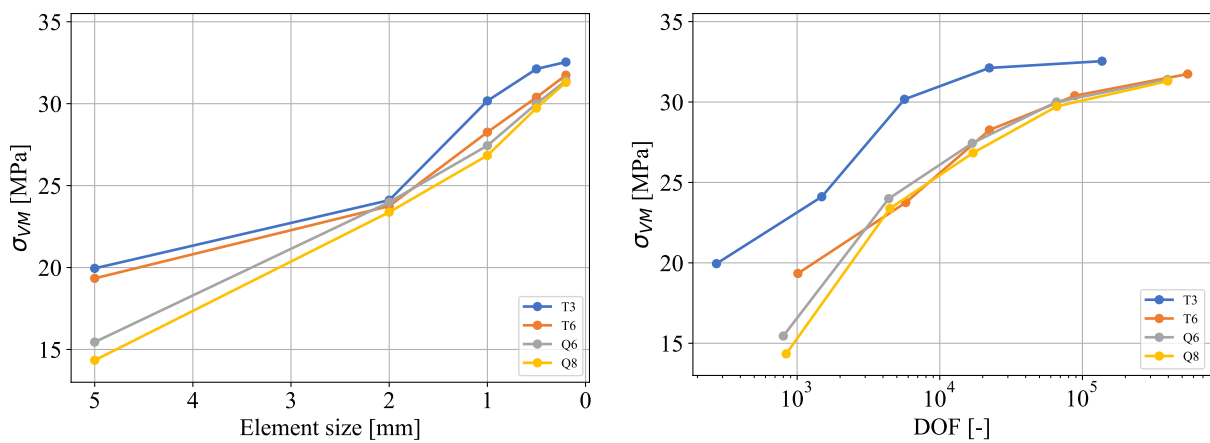


Figure 2.12: Von Mises stress as a function of element size (left) and the number of degrees of freedom (right).

The graph according to the size of the elements shows us a convergence or rather a decrease of the gaps between the different curves. Indeed, the second graph shows that the value of the maximum constraint is not the same for each curve. This is expected by the simple fact that we are using a coarse mesh,, *i.e.* it has not yet been refined sufficiently.

Finally, from a theoretical point of view, the refinement of the mesh (either by decreasing the size of the elements or by increasing the number of degrees of freedom) makes it possible to have values that converge towards a finite value for all types of elements. This is reassuring for the consistency of the results.

### 2.8.2 Displacements

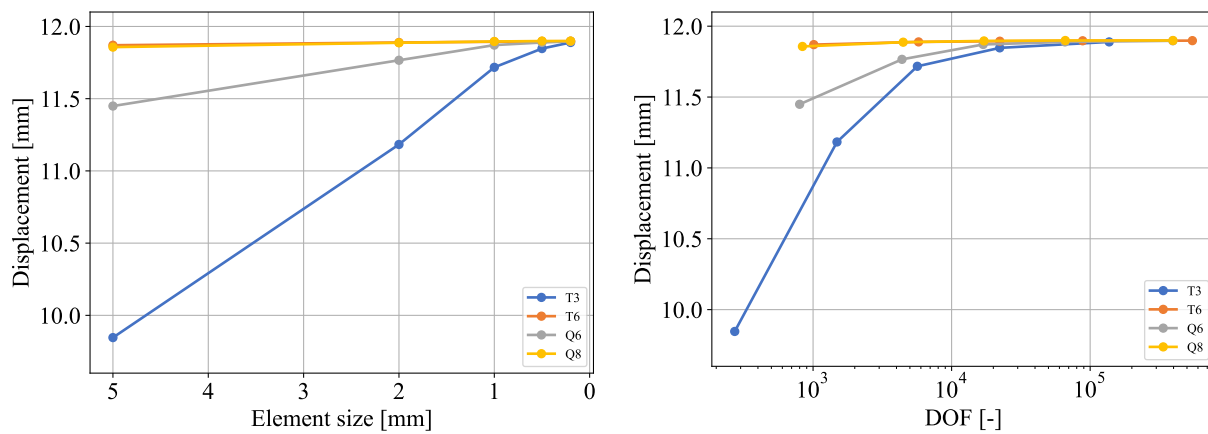


Figure 2.13: Displacement as a function of the element size (left) and the number of degrees of freedom (right).

These graphs resemble the area graphs established in the previous sections. It can be seen that the displacements for quadratic type elements are almost constant and therefore have an accuracy that does not change as a function of number of degrees of freedom, and therefore the size of the element (in the range from zero to five millimeters). For linear elements, the growth of the maximum displacement values tend to a finite value. The explanation of the difference between these two types of elements is the same as for the geometry. The quadratic type elements deform better to fit the geometry and therefore the displacement.

### 2.9 Influence of the number of degrees of freedom

An important factor that needs to be taken into account when evaluating the different elements is the computational complexity and the impacted CPU time. In this specific case, since the mechanical problem regards a single component with a relatively simple geometry, the simulation duration is in the order of seconds. For industrial applications, conversely, employing a computationally heavy element may require unfeasible simulation time, making this factor crucial when selecting the appropriate element.

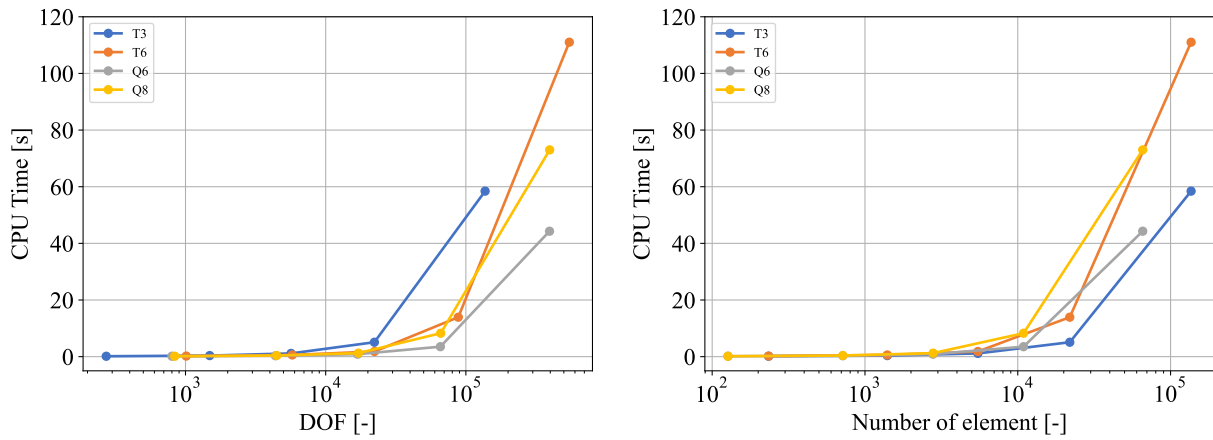


Figure 2.14: CPU time as a function of the number of degrees of freedom (left) and of the number of elements (right).

Fig. 2.14 illustrates a comparison of the CPU time for each element presented above. As expected, the duration (in seconds) of a simulation increases quadratically with respect to the number of degrees of freedom, *i.e.* the mesh refinement. Furthermore, T6 and Q8 manifest an heavier CPU load, which becomes more evident with an increase in DOFs : this is due to the quadratic assumed displacement field of the elements, that involves more parameters to be computed. Equivalent considerations are obtained analysing the CPU time as a function of the number of elements. For the analysis conducted here Q6 is the most computationally efficient element type, with a simulation conducted on the finest mesh lasting on average 14.6 seconds.

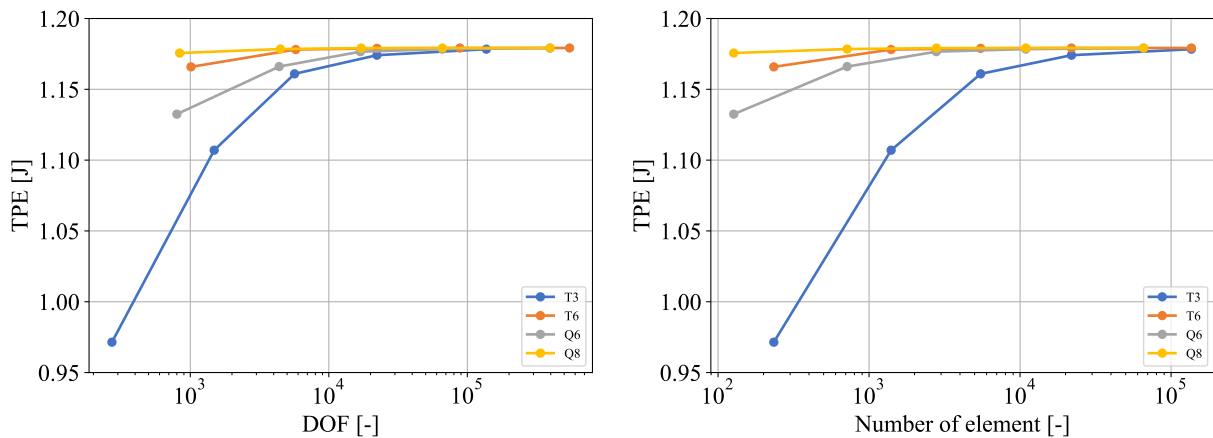


Figure 2.15: Total Potential Energy (TPE) as a function of the number of degrees of freedom (left) and of the number of elements (right).

The way the number of degrees of freedom influences the simulation can also be appreciated from the graph of the Total Potential Energy, in Fig. 2.15. As expected such graph reaches convergence and approaches the same value as in Fig. 2.6 : most relevantly, convergence is reached at different rates depending on the element. T3 and Q6, being simpler

linear elements, converge slower comparing to T6 AND Q8, which assume quadratic internal displacements.

## 2.10 Choice of the best element

The *best* element is the one that allows for the best compromise between the convergence speed and the accuracy of the TPE. The choice will be made thanks to the comparisons that have been made in the preceding graphs.

The T3 element can be excluded since it is the element for which the convergence of the TPE is the slowest (see Fig. 2.6 and Fig. 2.15), as is the case for the convergence of the maximum displacement with this same element (see Fig. 2.13). The second slowest element in terms of convergence of the TPE and the displacement is the Q6 element. However, it is relatively close to the T6 and Q8. The higher order elements (T6 and Q8) are very close to each other and converge faster in terms of TPE and displacement. Nevertheless, the CPU time required for the convergence of these elements is very high compared with lower order elements (T3 and Q6). This make the T6 and Q8 elements not efficient when a large number of elements/DOF is used (see Fig. 2.14).

It can be concluded that the Q6 is the *best* element for the claw structure as it combines fast convergence and short CPU time. It can also be noted that the element that performs better depends on the structure and the meshing. Thus, the discussion above is only valid for the claw with an automatic meshing.

## 2.11 Maximum admissible load

The main objective of this analysis is to find the maximum load to be applied to the claw (as depicted in Fig. 0.1) in order to keep the mechanical behavior inside of the elastic domain. More specifically, the goal is to find the value of the maximum applied force  $P_{\max}$  such that the value of the Von Mises stress remains below  $\sigma_{\text{yield}} = 50 \text{ MPa}$ .

In order to find the value of  $P_{\max}$  precisely and efficiently (hence, while employing as few simulations as possible), the analysis is conducted with the bisection method, an iterative algorithm that guesses the load at the generic  $k$ -th iteration  $P_k$  as :

$$P_k = \begin{cases} \frac{P_{k-1} + P_{k-2}}{2} & \text{if } \bar{\sigma}_{\text{VM}}(P_{k-1})\bar{\sigma}_{\text{VM}}(P_{k-2}) < 0, \\ \frac{P_{k-1} + P_{k-N}}{2} & \text{if } \bar{\sigma}_{\text{VM}}(P_{k-1})\bar{\sigma}_{\text{VM}}(P_{k-2}) > 0, \end{cases} \quad (2.9)$$

where  $\bar{\sigma}_{\text{VM}}(P_k)$  is defined as :

$$\bar{\sigma}_{\text{VM}}(P_k) = \sigma_{\text{VM}}(P_k) - \sigma_{\text{yield}}, \quad (2.10)$$

i.e. the difference between the maximum Von Mises stress in the claw obtained from the generic  $k$ -th simulation conducted with a load equal to  $P_k$  and the yield stress. Also,  $P_{k-N}$  is the last value of the load generating a  $\bar{\sigma}_{\text{VM}}(P_k)$  of opposite sign. A detailed overview of the method is proposed by Burden and Faires (1985) [5].

The initial values  $P_1$  and  $P_2$  are arbitrary values chosen in order to satisfy :

$$\begin{cases} \sigma_{VM}(P_1) < \sigma_{yield}, \\ \sigma_{VM}(P_2) > \sigma_{yield}, \end{cases} \quad (2.11)$$

and in this specific case are set to  $P_1 = 100$  N and  $P_2 = 200$  N. The termination of the iterative algorithm is, in this case, specified in terms of number of iterations.

A summary of the bisection algorithm is reported in Fig. 2.16 : ten iterations have been performed, with an applied load converging to 159.0 N and generating a maximum Von Mises stress of 49.92 MPa, which is just below the yield stress of the material.

The analysis from Mechanics of Materials yielded, from Eq. 1.22 on which our computer simulations were based, a value of  $P_{max} = 46.32$  N, which is almost four times smaller than the value calculated by the finite element simulations. This is easy to understand, mainly for two reasons. First of all, let us remind once more that the analytical solving of the problem was made possible by imposing a series of simplifying assumptions which evidently came at the expense of the accuracy of our results. Secondly, one of our assumptions was that the vast majority of the applied forces were concentrated to the horizontal beam which had a constant cross-section, while they are much more distributed in the claw given its geometry. It is trivial that the claw will therefore resist better than the simplified object we made.

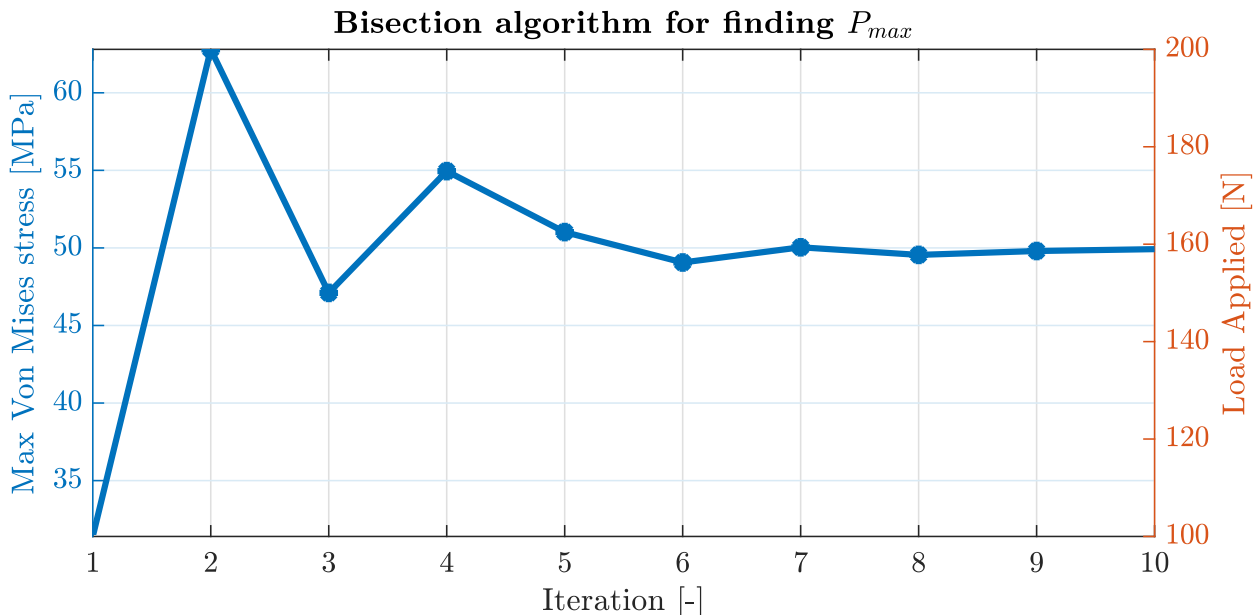


Figure 2.16: Convergence of the bisection algorithm used for finding the maximum applied load. The orange vertical scale on the right indicates the force applied in the simulation, the blue vertical scale on the left indicates the resulting max  $\sigma_{VM}$ .

## 2.12 Advanced meshing

The results and the considerations presented up until this section refer to simulations where the geometry has been discretized with coarse meshes generated automatically by the software. Such discretization instantiates elements with uniform sizes and doesn't account for

possible singularities in the result or regions where the stress gradient is high, situations which require local refinements.

More advanced meshes may be developed with *a posteriori* knowledge about the stress field generated in the claw, which is obtained in first approximations from the simulations with default coarse meshes. The discretization employed in advanced meshes heavily relies on the user involvement, skill and expertise, as the process can only be partially automated on the software side.

Results from the simulations with coarse meshes showed, as expected from the loading configuration and from the geometry, high stress gradients in the region near the tip of the claw. This preliminary result renders clear how the default mesh, characterized by elements with uniform size over the whole geometry, isn't ideal for this kind of mechanical problem.

In this section, two ways to improve the mesh will be presented. The first one via a *biasing on edge* and a second one with a *splitting of the body*. Particular attention will be paid to the convergence of the results in order to show quantitatively the best convergence of this *advanced mesh*.

### 2.12.1 Biasing on edge

To remedy the problem of coarse mesh, a « biased » mesh is developed with the objective of producing larger elements near the base of the claw and smaller elements near the tip. Such configuration is achieved by constraining the number of elements on the two straight edges to be equal and by unbalancing the density of elements on the curved sides : the mesh resulting from these constraints will be denser near the tip of the claw compared to its base.

Exploratory considerations were obtained by biasing the two curved edges as a whole, as in Fig. 2.17, where there is a smooth and continuous decrease in the element size towards the claw tip. Nevertheless, due to the peculiar morphology of the claw, this approach produces bad quality element in direct proximity of the tip, mostly in terms of an out-of-range skew angle : this phenomenon is accentuated with the quad element, but it's also present with the triangulairs. Analysis will show if simulations converge to the right values of the maximum stress and of the area.

A method similar to subsection 3.5 will be followed. The data from the simulations in Q3 and Q8 are taken and new mesh configurations are simulated. To do this, the biasing on edge is adapted to have the same number of elements (and degrees of freedom), so that results can be played on the same graph for the same element. The data collection is stopped when one of the meshes has reached the value at which the simulations of section 3.5 converged. The results are presented on the Fig. 2.17.

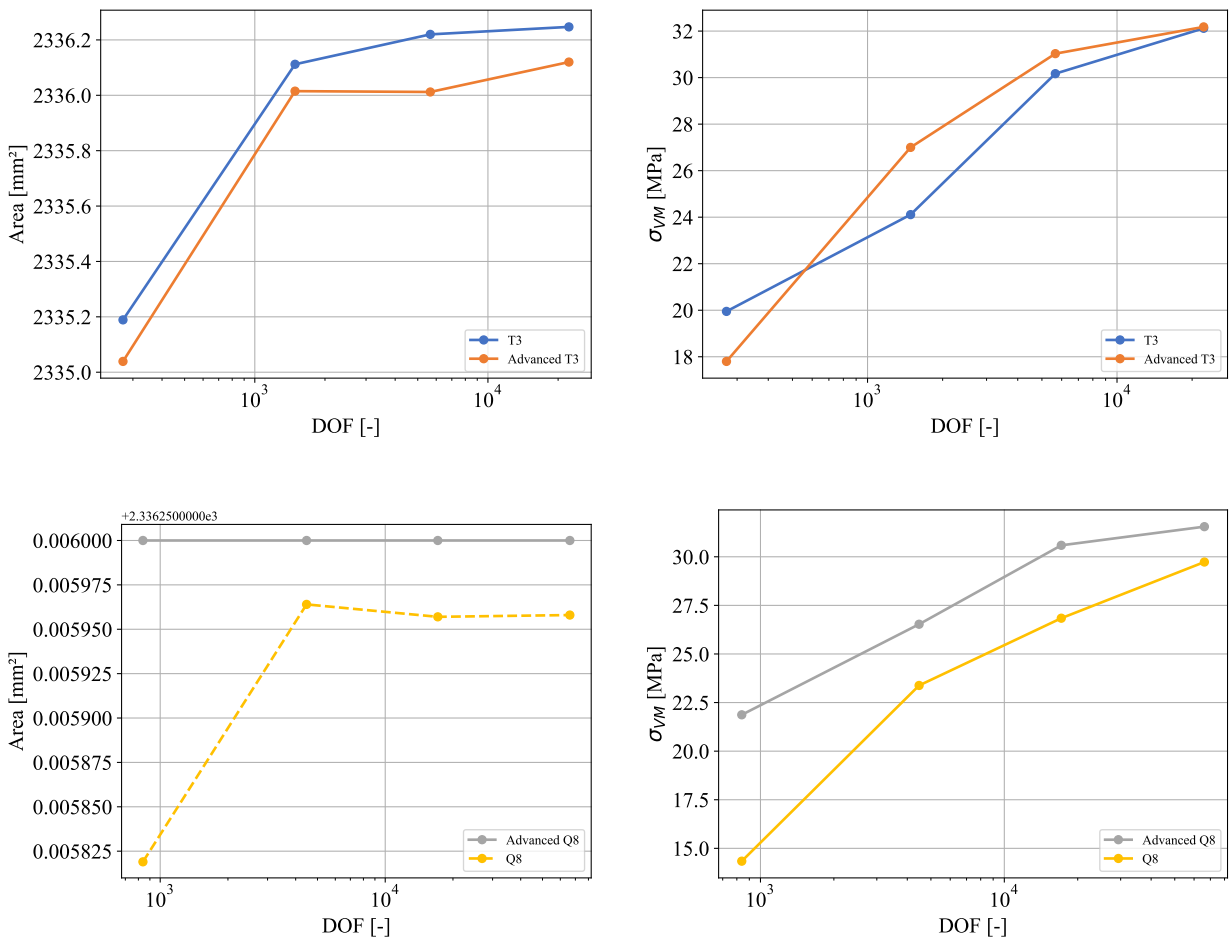


Figure 2.17: Convergence tests for area and maximum Von Mises stress in coarse and advance meshes of T3 (top) and Q8 (bottom) elements (biased on edge). The collection of the points is stopped when one of the simulations reaches the expected converged value.

The graphs in Fig. 2.17 confirm the qualitative conclusion. The simulations via an advanced mesh show a faster convergence. They reach a good approximation of the value for a lower number of elements (and thus of degrees of freedom). The mesh is therefore improved when constraints are applied to it at the places of interest (see beginning of section).

**Remark.** The previous results are obviously valid. For example, the convergence of quadratic elements for air is much more efficient than for triangular elements.

### 2.12.2 Sub-meshing

A refinement of the mesh is also possible via splitting. This consists in a manual division of the geometry into *sub-regions*. Then, each of the parts is meshed separately so that the final mesh is more accurate at the narrowest end of the claw. This concept is illustrated in Fig. 2.18, where the advanced meshes obtained via splitting are compared with the default coarse ones.

To do this optimally, the user is heavily involved and should parse the geometry in a

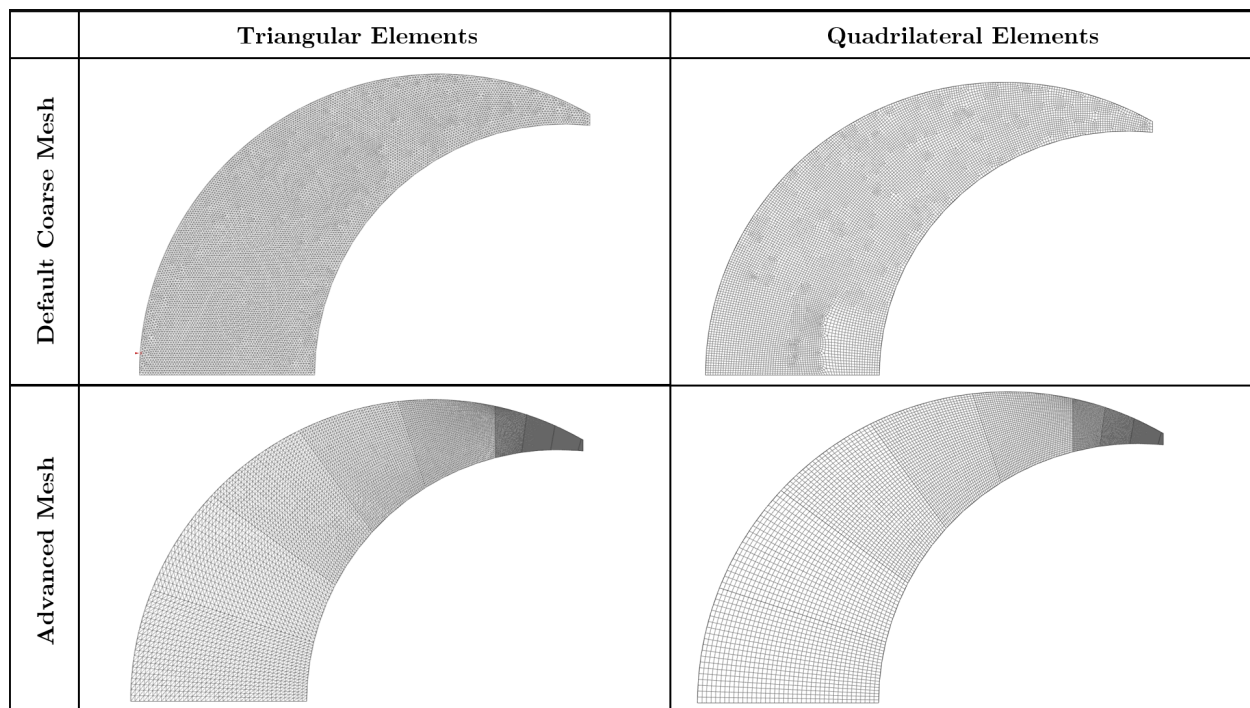


Figure 2.18: Comparison of coarse and advanced meshes with triangular and quadrilateral elements.

*trial-and-error* approach, constantly checking the element quality and tweaking the sub-mesh geometries and meshing parameters. Fig. 2.19 and Fig. 2.20 show a detail of this advanced meshing strategy for both triangular and quadrilateral elements and the results of the respective simulations.

In order to evaluate the effectiveness of an advanced meshing stage, results from a simulation with the mesh described above have been compared with the ones obtained from a default coarse mesh, the size of which has been chosen closest to the average element size. The meshes and the resulting stress fields are shown in Fig. 2.20 and Fig. 2.19 : it's immediately noticeable that the advanced mesh renders the stress field smoother. Moreover the maximum Von Mises stress in this case (31.73 MPa) is closer to the average convergence value obtained from coarse meshes (Fig. 2.7) ; the maximum  $\sigma_{VM}$  for the coarse mesh is 29.73 MPa. Equivalent results are obtained from the advanced triangular mesh, as in Fig. 2.19.

The improvement in the element quality is depicted in Table 2.5, reporting the number of elements failing the quality check in terms of the parameters already described in Section 2.7. Generally, both tri and quad meshes grant a lower fraction of improper elements, which for the advanced meshes are generally located solely in the close proximity of the claw tip, where the edges of the geometry are far from perpendicular : this factor induces a generation of elements with sub-optimal skew angles.

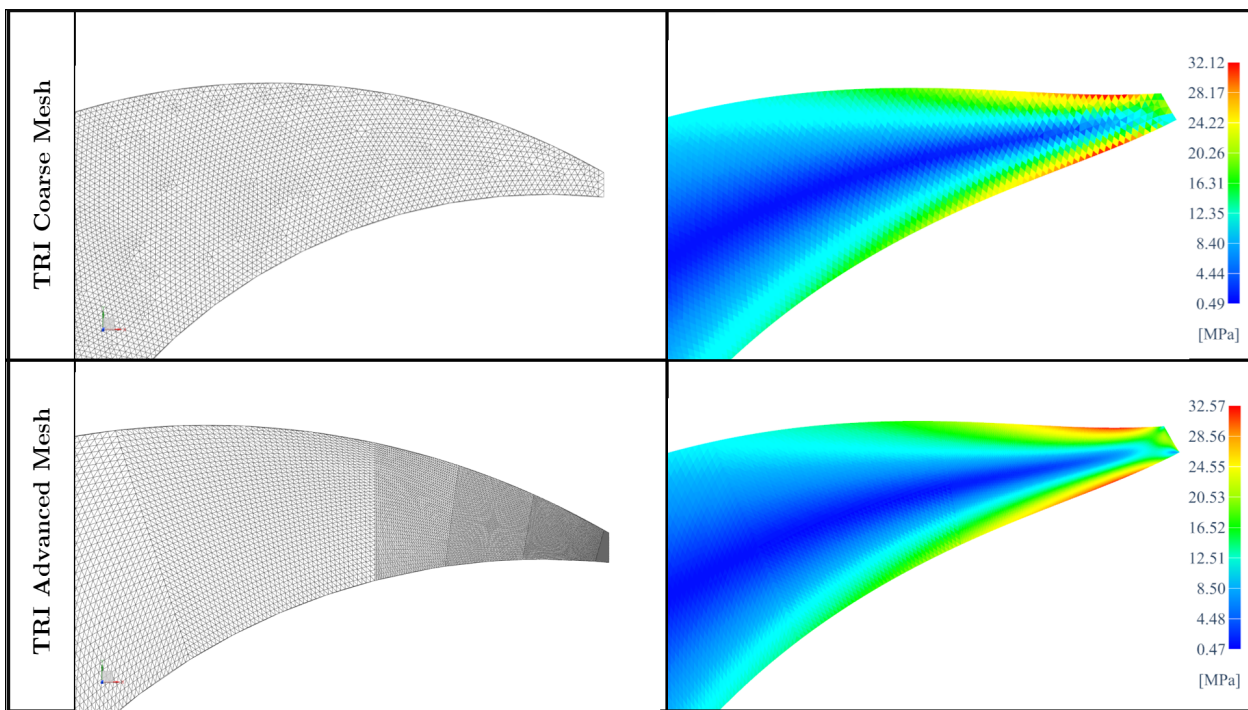


Figure 2.19: Stress fields from simulations with the mesh generated by default from the software (top) and with TRI-advanced mesh implemented by the user (bottom).

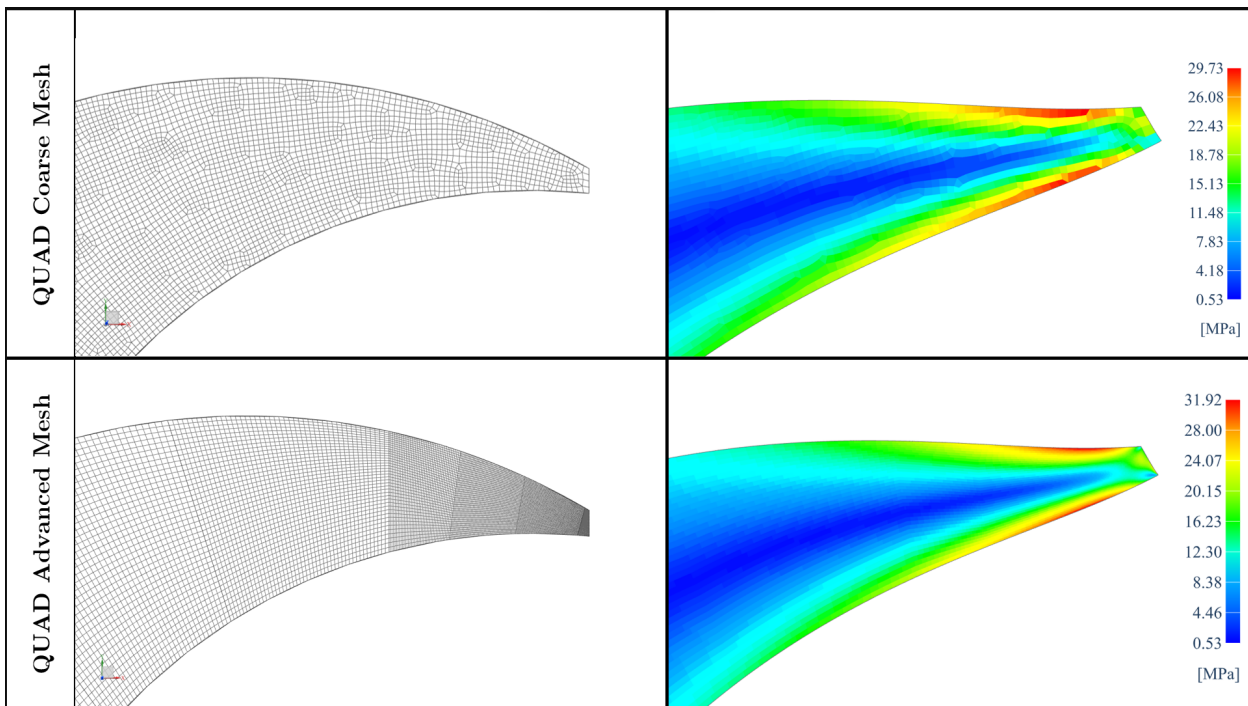


Figure 2.20: Stress fields from simulations with the mesh generated by default from the software (top) and with QUAD-advanced mesh implemented by the user (bottom).

A further significant improvement introduced from the advanced mesh is a noticeable reduction in the number of degrees of freedom, as Table 2.5 illustrates. Advanced meshes

Geometry	Triangular		Quadrilateral	
Mesh	Default	Advanced	Default	Advanced
<b>Jacobian Sign</b>	0%	0%	0%	0%
<b>Jacobian Ratio</b>	0%	0%	0%	0%
<b>Aspect Ratio</b>	0%	0%	0%	0%
<b>Skew Angle</b>	1.47%	73.25%	2.78%	1.04%
<b>Degrees of freedom</b>	21898	10000	391368	77104

Table 2.5: Increase in element quality with advanced meshes. Data is reported as the percentage of *out-of-range* elements over the total number of elements in the mesh.

not only introduce less degrees of freedom to the problem improving the CPU time, but crucially they allow to optimally « allocate » such computations in regions where they are required. In the specific case of the claw, the advanced mesh granted the correct resolution required for grasping the complex stress patterns near the tip, while still maintaining low the number of DOFs of the problem.

### 3 Optimization

Both the geometry and the dimensions of the claw may be adjusted in order to increase the maximum possible load in the elastic domain. In this specific case, adjustments are allowed only if the increase in the claw volume (or area, given the uniform thickness) is less than +5%.

The analytical solution proposed in Section 1 concluded that, as in Eq. 1.20, Eq. 1.21 and 1.22, an inverse proportionality relationship subsists between the stress and the geometry of the cross section, expressed in terms of its area and its moment of inertia. From this, it is deduced that an increase in the area and the moment of inertia will result in an overall decrease of the Von Mises stress : since the assumed thickness of the plane stress problem is fixed and equal to 5 mm, adjustments have to be made to the height of the cross-section (dimension «  $d_1$  » in Fig. 1.3). For this purpose, the radii of external and internal curved edges of the claw have been adjusted of +1 mm and -1 mm respectively, as shown in Fig. 3.1. As a consequence, the resistive cross section and the moment of inertia are increased, lowering the Von Mises stress and therefore allowing for higher loads. The volume of the claw increased from  $11681.28 \text{ mm}^3$  (2D area of  $2336.256 \text{ mm}^2$ ) for the non-optimized geometry to  $12216.80 \text{ mm}^3$  (2D area of  $2443.36 \text{ mm}^2$ ) for the optimized one, consisting in a variation of +4.58%, in range with the requirements.

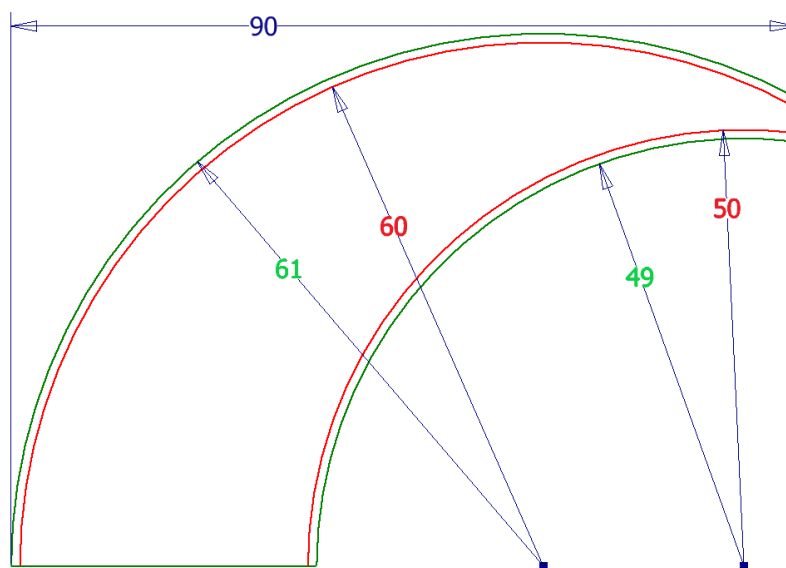


Figure 3.1: The original geometry (in red) compared with the new optimized geometry (in green).

The maximum allowed load in elastic domain is expected to increase in comparison to the one allowed by the non-optimized geometry : this statement is assessed and quantified with a bisection algorithm [5] conducted in ten iterations and with a mesh generated with the same properties than the one employed to find the maximum load previously (see section 2.11). Fig. 3.2 recapitulates the convergence of the algorithm, which stabilizes to a much higher value of the admissible load :  $P_{\max, \text{opt}} = 250.30 \text{ MPa}$ , with an increase of +57.42% with respect to the load obtained from the previous analysis ( $P_{\max, \text{non-opt}} = 159.30 \text{ MPa}$ ).

It is therefore concluded that the optimized geometry of the claw increases the maximum admissible load without excessively increasing the volume of the component.

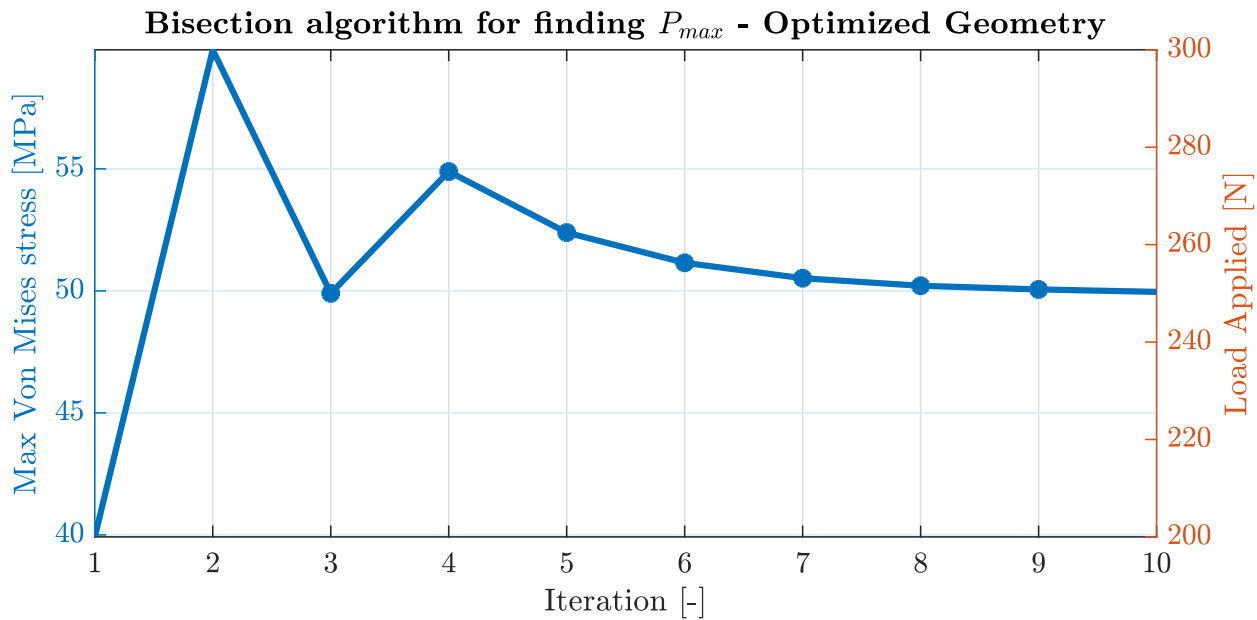


Figure 3.2: Convergence of the bisection algorithm used for finding the maximum applied load with the optimized geometry. The orange vertical scale on the right indicates the force applied in the simulation, the blue vertical scale on the left indicates the resulting max  $\sigma_{VM}$ .

## Conclusions

The scope of this work was to conduct a mechanical analysis of a loaded claw element by the means of the Finite Elements Method. A first inquiry was carried out analytically via a mechanics of material study, with the proper assumptions and simplifications, that led to preliminary results for the analysis.

Secondly, a Finite Element simulation is plain stress was conducted on Siemens NX, where four types of two-dimensional elements (T3, T6, Q6 and Q8) have been studied and compared, aiming at selecting the best element to be employed. Crucially, a singularity has been resolved by relocating the point load from the corner of the claw to the edge of the tip, and both local and global convergence have been assessed. Advanced meshing strategies have been employed as well, aiming at assessing their benefits on element quality and their influence on the resulting stress field. All the considerations drawn have been accounted in the main objective of the analysis, which is estimating the maximum admissible load of the claw in the bounds of the elastic domain.

Finally, an optimization is proposed : the geometry of the claw has been adjusted by increasing and decreasing the external and internal radii of the curved edges, respectively. As a consequence an higher maximum admissible load is allowed while still remaining in the elastic domain.

Special attention was given to the critique of the results. The simulations and analyses carried out seem to be coherent physically but also with respect to the course and the different links investigated.

## List of Figures

0.1	Representation of the claw (dimensions are given in mm) [1]. . . . .	4
1.1	Representation of the simplified model for the use of Mechanics of Materials	7
1.2	Schematic of the applied and reaction forces on the simplified claw. . . . .	8
1.3	Representation of the cross-section as well as the normal stress (green) and the bending stress (red). Notice that the latter reaches its maximum at the walls of the beam. . . . .	10
1.4	Photographic images of the bottom of a bovine hind limb claw with TTN obtained during application of a static load of 1 (A), 2 (B), and 3 (C) kN following image processing [2]. . . . .	12
1.5	Contour map of Von Mises stresses (units in GPa) on (a) the outer surface of the claw and (b) through the mid-section [3]. . . . .	13
1.6	Von Mises equivalent stresses with respect to the applied load. . . . .	14
1.7	Vertical deformation of the claw resulting of applied load with respect to the position $x$ in the horizontal beam of our simplified model. . . . .	14
2.1	Modeling of the claw using Siemens NX. . . . .	16
2.2	Schematic of the T3 finite element. . . . .	17
2.3	Schematic of the T6 finite element. . . . .	18
2.4	Schematic of the Q6 finite element. . . . .	18
2.5	Schematic of the Q8 finite element. . . . .	19
2.6	Global convergence - TPE as function of the element size. . . . .	20
2.7	Local convergence - $\sigma_{VM}$ as a function of the element size. . . . .	21
2.9	Modeling of the various stress components with NX. . . . .	23
2.10	Displacement profile in the claw according to our NX simulations. . . . .	24
2.11	Aberrant elements in a mesh with Q6 elements (left) and T6 elements (right). . . . .	27
2.12	Von Mises stress as a function of element size (left) and the number of degrees of freedom (right). . . . .	27
2.13	Displacement as a function of the element size (left) and the number of degrees of freedom (right). . . . .	28
2.14	CPU time as a function of the number of degrees of freedom (left) and of the number of elements (right). . . . .	29
2.15	Total Potential Energy (TPE) as a function of the number of degrees of freedom (left) and of the number of elements (right). . . . .	29
2.16	Convergence of the bisection algorithm used for finding the maximum applied load. The orange vertical scale on the right indicates the force applied in the simulation, the blue vertical scale on the left indicates the resulting max $\sigma_{VM}$ . . . . .	31
2.17	Convergence tests for area and maximum Von Mises stress in coarse and advance meshes of T3 (top) and Q8 (bottom) elements (biased on edge). The collection of the points is stopped when one of the simulations reaches the expected converged value. . . . .	33
2.18	Comparison of coarse and advanced meshes with triangular and quadrilateral elements. . . . .	34
2.19	Stress fields from simulations with the mesh generated by default from the software (top) and with TRI-advanced mesh implemented by the user (bottom). . . . .	35

2.20 Stress fields from simulations with the mesh generated by default from the software (top) and with QUAD-advanced mesh implemented by the user (bottom). . . . .	35
3.1 The original geometry (in red) compared with the new optimized geometry (in green). . . . .	37
3.2 Convergence of the bisection algorithm used for finding the maximum applied load with the optimized geometry. The orange vertical scale on the right indicates the force applied in the simulation, the blue vertical scale on the left indicates the resulting max $\sigma_{VM}$ . . . . .	38

## List of Tables

2.1 Surface of the claw as approximated by meshing with different elements . . . . .	22
2.2 Worst values of element quality parameters for T3 elements. . . . .	25
2.3 Worst values of element quality parameters for T6 elements. . . . .	25
2.4 Worst values of element quality parameters for Q6 and Q8 elements. . . . .	26
2.5 Increase in element quality with advanced meshes. Data is reported as the percentage of <i>out-of-range</i> elements over the total number of elements in the mesh. . . . .	36

## References

- [1] J.-P. Ponthot. *MECA0036-2 Finite Element Method*. 2020-2021. University of Liege.
- [2] S.D. Noble J.D. D. Johnston, D.J. R. Eichhorn, S.A. Kontulainen and M.D. Jelinski. *Investigation of white line separation under load in bovine claws with and without toe-tip necrosis*. Aug 2019. American Journal of Veterinary Research.
- [3] M.R. Johnson P.J. Withers W.I. Sellers P.L. Falkingham P.M. Mummery P.M. Barett D.R. Raymont P.L. Manning, L. Margetts. *Biomechanics of Dromaeosaurid Dinosaur Claws: Application of X-Ray Microtomography, Nanoindentation, and Finite Element Analysis*. 2009. Anatomical record.
- [4] King-Hay Yang. *Basic Finite Element Method as Applied to Injury Biomechanics*. 2018. Book.
- [5] J.D. Faires R. Burden. *Numerical analysis*, pages 28–31. 1985.